



TOI-824 b: A New Planet on the Lower Edge of the Hot Neptune Desert

Jennifer A. Burt^{1,2,33}, Louise D. Nielsen³, Samuel N. Quinn⁴, Eric E. Mamajek¹, Elisabeth C. Matthews², George Zhou⁴, Julia V. Seidel³, Chelsea X. Huang^{2,33}, Eric Lopez⁵, Maritza Soto⁶, Jon Otegi^{3,7}, Keivan G. Stassun^{8,9}, Laura Kreidberg^{4,34}, Karen A. Collins⁴, Jason D. Eastman⁴, Joseph E. Rodriguez¹⁰, Andrew Vanderburg¹¹, Samuel P. Halverson¹, Johanna K. Teske^{12,35}, Sharon X. Wang¹², R. Paul Butler¹³, François Bouchy³, Xavier Dumusque³, Damien Segransen³, Stephen A. Shtetman¹², Jeffrey D. Crane¹², Fabo Feng¹³, Benjamin T. Montet¹⁴, Adina D. Feinstein^{15,36}, Yuri Beletski¹⁶, Erin Flowers^{17,36}, Maximilian N. Günther^{2,33}, Tansu Daylan^{2,37}, Kevin I. Collins¹⁸, Dennis M. Conti¹⁹, Tianjun Gan²⁰, Eric L. N. Jensen²¹, John F. Kielkopf²², Thiam-Guan Tan²³, Ravit Helled⁷, Caroline Dorn⁷, Jonas Haldemann²⁴, Jack J. Lissauer²⁵, George R. Ricker², Roland Vanderspek², David W. Latham⁴, S. Seager^{2,26,27}, Joshua N. Winn¹⁷, Jon M. Jenkins²⁸, Joseph D. Twicken^{28,29}, Jeffrey C. Smith^{28,29}, Peter Tenenbaum^{28,29}, Scott Cartwright³⁰, Thomas Barclay^{5,31}, Joshua Pepper³², Gilbert Esquerdo⁴, and William Fong²

¹ Jet Propulsion Laboratory, California Institute of Technology, 4800 Oak Grove Drive, Pasadena, CA 91109, USA

² Department of Physics and Kavli Institute for Astrophysics and Space Research, Massachusetts Institute of Technology, Cambridge, MA 02139, USA

³ Observatoire de l'Université de Genève, 51 Chemin des Maillettes, 1290 Versoix, Switzerland

⁴ Center for Astrophysics | Harvard & Smithsonian, 60 Garden Street, Cambridge, MA 02138, USA

⁵ NASA Goddard Space Flight Center, 8800 Greenbelt Road, Greenbelt, MD 20771, USA

⁶ School of Physics and Astronomy, Queen Mary University London, 327 Mile End Road, London E1 4NS, UK

⁷ Institute for Computational Science, University of Zurich, Winterthurerstr. 190, CH-8057 Zurich, Switzerland

⁸ Department of Physics and Astronomy, Vanderbilt University, Nashville, TN 37235, USA

⁹ Department of Physics, Fisk University, Nashville, TN 37208, USA

¹⁰ Harvard-Smithsonian Center for Astrophysics, Harvard University, Cambridge, MA 02138, USA

¹¹ Department of Astronomy, University of Wisconsin-Madison, Madison, WI 53706, USA

¹² The Observatories of the Carnegie Institution for Science, 813 Santa Barbara Street, Pasadena, CA 91101, USA

¹³ Earth & Planets Laboratory, Carnegie Institution for Science, 5241 Broad Branch Road, NW, Washington, DC 20015, USA

¹⁴ School of Physics, The University of New South Wales, Sydney, NSW 2052, Australia

¹⁵ The Department of Astronomy and Astrophysics, The University of Chicago, 5640 S. Ellis Avenue, Chicago, IL 60637, USA

¹⁶ Las Campanas Observatory, Vallenar, Atacama, Chile

¹⁷ Department of Astrophysical Sciences, Princeton University, 4 Ivy Lane, Princeton, NJ 08544, USA

¹⁸ George Mason University, 4400 University Drive, Fairfax, VA, 22030, USA

¹⁹ American Association of Variable Star Observers, 49 Bay State Road, Cambridge, MA 02138, USA

²⁰ Department of Astronomy and Tsinghua Centre for Astrophysics, Tsinghua University, Beijing 100084, People's Republic of China

²¹ Dept. of Physics & Astronomy, Swarthmore College, Swarthmore PA 19081, USA

²² Department of Physics and Astronomy, University of Louisville, Louisville, KY 40292, USA

²³ Perth Exoplanet Survey Telescope, Perth, Western Australia, Australia

²⁴ Department of Space Research & Planetary Sciences, University of Bern, Gesellschaftsstrasse 6, CH-3012 Bern, Switzerland

²⁵ Space Science & Astrobiology Division, MS 245-3, NASA Ames Research Center, Moffett Field, CA 94035, USA

²⁶ Department of Earth, Atmospheric and Planetary Sciences, Massachusetts Institute of Technology, Cambridge, MA 02139, USA

²⁷ Department of Aeronautics and Astronautics, MIT, 77 Massachusetts Avenue, Cambridge, MA 02139, USA

²⁸ NASA Ames Research Center, Moffett Field, CA, 94035, USA

²⁹ SETI Institute, Mountain View, CA 94043, USA

³⁰ Proto-Logic LLC, 1718 Euclid Street NW, Washington, DC 20009, USA

³¹ University of Maryland, Baltimore County, 1000 Hilltop Circle, Baltimore, MD 21250, USA

³² Department of Physics, Lehigh University, 16 Memorial Drive East, Bethlehem, PA 18015, USA

Received 2020 February 5; revised 2020 July 23; accepted 2020 August 2; published 2020 September 4

Abstract

We report the detection of a transiting hot Neptune exoplanet orbiting TOI-824 (SCR J1448-5735), a nearby ($d = 64$ pc) K4V star, using data from the Transiting Exoplanet Survey Satellite. The newly discovered planet has a radius $R_p = 2.93 \pm 0.20 R_\oplus$ and an orbital period of 1.393 days. Radial velocity measurements using the Planet Finder Spectrograph and the High Accuracy Radial velocity Planet Searcher spectrograph confirm the existence of the planet, and we estimate its mass to be $18.47 \pm 1.84 M_\oplus$. The planet's mean density is $\rho_p = 4.03_{-0.78}^{+0.98} \text{ g cm}^{-3}$, making it more than twice as dense as Neptune. TOI-824 b's high equilibrium temperature makes the planet likely to have a cloud-free atmosphere, and thus it is an excellent candidate for follow-up atmospheric studies. The detectability of TOI-824 b's atmosphere from both ground and space is promising and could lead to the detailed characterization of the most irradiated small planet at the edge of the hot Neptune desert that has retained its atmosphere to date.

Unified Astronomy Thesaurus concepts: Exoplanet astronomy (486); Exoplanet detection methods (489); Exoplanets (498); Transit photometry (1709); Radial velocity (1332); Stellar properties (1624)

³³ Juan Carlos Torres Fellow.

³⁴ Clay Fellow.

³⁵ NASA Hubble Fellow.

³⁶ NSF Graduate Research Fellow.

³⁷ Kavli Fellow.

1. Introduction

The Transiting Exoplanet Survey Satellite (TESS; Ricker et al. 2015) spent the first year of its mission searching for planets orbiting cool, nearby stars in the Ecliptic Southern

Hemisphere. To date, the TESS mission has detected over 1000 planet candidates and has significantly expanded the number of small planets detected around cool stars (see, e.g., Dragomir et al. 2019; Günther et al. 2019; Kostov et al. 2019).

There are a number of striking planet populations that emerge when studying the period and radius measurements that TESS and its predecessor Kepler have compiled for the 2000+ confirmed transiting exoplanets they detected. One of the most surprising is the huge population of planets between the size of Earth and Neptune that orbit stars of all stellar types (Coughlin et al. 2016), a population that is missing from our own solar system. Equally interesting and enigmatic are the hot Jupiters that orbit their stars with periods thousands of times shorter than our own Jupiter (e.g., Mayor & Queloz 1995) and the small, tightly packed transiting planets around FGKM dwarfs that often exist in low mutual inclination systems just wide of orbital resonance chains (Lissauer et al. 2011; Burke et al. 2014). At the same time, this sizeable data set reveals the lack of planets within certain regions of parameter space. One notable example is the existence of the “hot Neptune desert,” or the lack of planets the size and mass of Neptune on periods shorter than 4 days that is seen in both transit and Doppler detections (Szabó & Kiss 2011; Mazeh et al. 2016). This desert cannot be a result of observational bias as Kepler, TESS, and various radial velocity (RV) surveys have detected a plethora of planets with masses and radii similar to Neptune on much longer period orbits, which have lower transit detection probabilities and smaller RV semiamplitudes (Lecavelier Des Etangs 2007; Beaugé & Nesvorný 2013). Thus these hot Neptunes must be intrinsically rare, and indeed analysis of the Kepler DR25 planet candidates suggests that $<1\%$ of FGK stars host planets that have radii in the range of $2\text{--}6 R_{\oplus}$ on orbits shorter than 4 days (Hsu et al. 2019).

The origin of these hot Neptunes remains unclear as their radii lie between the terrestrial planets that are thought to form primarily in situ (Matsumoto & Kokubo 2017) and the giant planets that astronomers have traditionally believed must form out past the snow line before migrating inward (Nelson et al. 2017).

Two characteristics that have been noted are that hot Neptunes, much like hot Jupiters, are more likely to be found around metal-rich stars and are more likely to be found in systems where they are the only transiting planet (Dong et al. 2018; Petigura et al. 2018). Determining whether or not these similarities suggest a common method of origin or migration history between the two hot planet populations requires the detection and confirmation of enough hot Neptunes to identify which planetary, atmospheric, and orbital characteristics are common across hot Neptunes and which vary from planet to planet. Thanks to the inherent rarity of these planets in the Milky Way, the only way to compile such a set is to search a very large number of stars for evidence of hot Neptunes. Such a survey is impractical for RV instruments, where only one star can be observed at a time. Even Kepler, which studied over 100,000 stars at a precision level that should easily detect such planets, discovered only a handful (Hsu et al. 2019). With its high level of photometric precision and an observing plan that will tile over 70% of the night sky for at least 28 days during its primary and extended missions, TESS is an ideal mission to detect hot Neptunes. Indeed, during its first year alone, the mission has already added three verified hot Neptune planets in the exoplanet databases (Díaz et al. 2020; Esposito et al. 2019,

and this work) and identified over 100 additional hot Neptune planet candidates that await confirmation.³⁸

Here we report the discovery of a hot Neptune orbiting TOI-824, a nearby ($d = 64$ pc) K4 dwarf star located in the constellation of Circinus. This paper is organized as follows. In Section 2 we describe the variety of data sets used to characterize TOI-824 and its planet. In Section 3 we detail the analysis of these data sets, culminating in the use of the EXOFASTv2 software package to determine the system’s stellar, orbital, and planetary parameters. In Section 4 we detail how including ground-based photometry in our fits revealed that the initial Science Processing Operations Center (SPOC) radius estimate for TOI-824 b was $\sim 11\%$ too large, and we outline suggestions for future TESS follow-up efforts focusing on stars in crowded regions of the sky. Finally, we conclude in Section 5 with a discussion of the planet’s likely interior composition, the atmospheric retention capabilities of this and other hot Neptune planets, and TOI-824 b’s potential for future atmospheric characterization efforts.

2. Data

2.1. Astrometry and Photometry

TOI-824 (SCR J1448-5735, TYC 8688-915-1, TIC 193641523, 2MASS J14483982-5735175) is a $V = 11.15$ (Winters et al. 2011) K-type dwarf star located at 64.4 ± 0.03 pc ($\varpi = 15.6142 \pm 0.0348$ mas; Gaia Collaboration et al. 2018). The star has not drawn much previous attention, having been first pointed out as a high-proper-motion, potentially nearby star by Finch et al. (2007; identified as SCR J1448-5735). As the star had a preliminary photometric distance estimate of only 18 pc by Finch et al. (2007), Winters et al. (2011) measured Krons–Cousins *VRI* photometry as part of the SuperCOSMOS RECONS survey and provided an updated distance estimate of 62.4 ± 9.7 pc, not far from the current Gaia DR2 estimate (Bailer-Jones et al. 2018). Astrometry and photometry for TOI-824 are summarized in Table 1. The star’s position, proper motion, parallax, and Gaia photometry are drawn from Gaia DR2. Optical photometry is adopted from Tycho-2 ($B_T V_T$; Høg et al. 2000), APASS DR9 ($BVr“i”$; Henden et al. 2015, 2016), and Gaia DR2 (Gaia Collaboration et al. 2018), while infrared photometry is adopted from the Two Micron All Sky Survey (2MASS; *JHK_s*; Cutri et al. 2003) and the Wide-field Infrared Survey Explorer (WISE; Cutri et al. 2012).

2.2. TESS Time Series Photometry

TOI-824 was observed by TESS from UT 2019 April 22 through 2019 May 20 as part of the Sector 11 campaign and again from UT 2019 May 21 through 2019 June 18 as part of Sector 12. The star fell on CCD 3 of Camera 2 during Sector 11 and then on CCD 4 of Camera 2 during Sector 12.

The SPOC data (Jenkins et al. 2016) for TOI-824, available at the the Mikulski Archive for Space Telescopes (MAST) website,³⁹ includes both simple aperture photometry (SAP) flux measurements (Twicken et al. 2010; Morris et al. 2017) and presearch data conditioned simple aperture photometry (PDCSAP) flux measurements (Smith et al. 2012; Stumpe et al. 2012, 2014). The instrumental variations present in the

³⁸ <https://tev.mit.edu/data/>

³⁹ <https://mast.stsci.edu>

Table 1
Stellar Parameters for TOI-824

Parameter	Value	Source
Designations	TIC 193641523 SCR J1448-5735 2MASS J14483982-5735175	Stassun et al. (2019) Finch et al. (2007) Cutri et al. (2003)
R.A. (hh:mm:ss)	14:48:39.71	Gaia DR2
Decl. (dd:mm:ss)	-57:35:19.92	Gaia DR2
μ R.A. (mas yr ⁻¹)	-51.6035 ± 0.068	Gaia DR2
μ Decl. (mas yr ⁻¹)	-152.392 ± 0.079	Gaia DR2
Parallax (mas)	15.696 ± 0.049	Gaia DR2 ^a
Distance (pc)	63.71 ± 0.20	Gaia DR2
SpT	K4V	This work
<i>B</i>	12.263 ± 0.005	APASS/DR9
<i>V</i>	11.153 ± 0.008	APASS/DR9
<i>V</i>	11.15 ± 0.03:	Winters et al. (2011)
<i>r'</i>	10.717 ± 0.025	APASS/DR9
<i>i'</i>	10.303 ± 0.053	APASS/DR9
TESS	10.0732 ± 0.006	TIC8
<i>G</i>	10.762 ^{+0.02} _{-0.001}	Gaia DR2
<i>G</i> _{BP}	11.406 ^{+0.02} _{-0.001}	Gaia DR2
<i>G</i> _{RP}	10.021 ^{+0.02} _{-0.001}	Gaia DR2
<i>J</i>	9.145 ± 0.018	2MASS
<i>H</i>	8.557 ± 0.046	2MASS
<i>K</i> _s	8.432 ± 0.038	2MASS
<i>W</i> ₁	8.154 ± 0.083	WISE
<i>W</i> ₂	8.326 ± 0.021	WISE
<i>W</i> ₃	6.948 ± 0.017	WISE
<i>W</i> ₄	3.372 ± 0.020	WISE
<i>U</i> (km s ⁻¹)	-0.220 ± 0.152	This work
<i>V</i> (km s ⁻¹)	-45.803 ± 0.181	This work
<i>W</i> (km s ⁻¹)	-33.886 ± 0.140	This work

Note.

^a Correction of +82 μ as applied to the Gaia parallax as per Stassun & Torres (2018).

SAP flux are removed in the PDCSAP result. At the start of each orbit, thermal effects and strong scattered light impact the systematic error removal in PDC (see TESS data release notes DRN16 and DNR17). Before the fitting process described in Section 3.8, we use the quality flags provided by SPOC to mask out unreliable segments of the time series. We then further detrend the TESS data set by breaking it into the individual spacecraft orbits (two per sector) and fitting each with a low-order spline to address residual trends in the light curve (Figure 1).

2.3. Ground-based Time-series Photometry

We acquired ground-based time-series follow-up photometry of TOI-824 during the times of transit predicted by the TESS data. We used the TESS Transit Finder, which is a customized version of the Tapir software package (Jensen 2013), to schedule our transit observations.

We observed a full transit of TOI-824 on UTC 2019 July 1 in the *R*_c band from the Perth Exoplanet Survey Telescope (PEST) near Perth, Australia. The 0.3 m telescope is equipped with a 1530 × 1020 SBIG ST-8XME camera with an image scale of 1''.2 pixel⁻¹, resulting in a 31' × 21' field of view. A custom pipeline based on C-Munipack⁴⁰ was used to

calibrate the images and extract differential photometry for TOI-824 and all other stars detected within 2''.5 of TOI-824, using apertures with radius 6''.2. The images have typical stellar point spread functions (PSFs) with an FWHM of 3''.6.

Four full transits of TOI-824 b were observed using the Las Cumbres Observatory Global Telescope (LCOGT) 1 m network (Brown et al. 2013) on UTC 2019 June 30, 2019 July 13, 2019 July 27, and 2019 August 5 in Pan-STARSS *z*, *B*, *B*, and Pan-STARSS *z* bands, respectively. All observations were obtained by the LCOGT node at Cerro Tololo Inter-American Observatory, except the August 5 observations, which were obtained by the LCOGT node at Siding Spring Observatory. The telescopes are equipped with 4096 × 4096 LCO SINISTRO cameras having an image scale of 0''.389 pixel⁻¹, resulting in a 26' × 26' field of view. The images were calibrated by the standard LCOGT BANZAI pipeline, and the photometric data were extracted using the AstroImageJ (AIJ) software package (Collins et al. 2017). Circular apertures with radius of 12 pixels (4''.7) were used to extract the differential photometry. The image sets have average stellar PSF FWHMs ranging from 1''.4 on August 5 to 2''.4 on July 14.

2.4. Spectroscopic Data

TOI-824 was observed by the CHIRON spectrograph (Tokovinin et al. 2013) to determine whether its stellar parameters were well suited to precision RV follow-up efforts. CHIRON is a high-resolution spectrograph fed by an image slicer and a fiber bundle, located on the 1.5 m SMARTS telescope at Cerro Tololo Inter-American Observatory (CTIO), Chile. CHIRON has a spectral resolving power of $R \simeq 80,000$ over the wavelength region from 4100 to 8700 Å. Two spectra were obtained for TOI-824 on UT 2019 July 5 and 6.

2.5. Imaging Data

We collected AO images with the Very Large Telescope (VLT)/NaCo on UT 2019 August 2 using the Br γ filter centered on 2.166 μ m (Lenzen et al. 2003; Rousset et al. 2003). We collected a total of nine frames, each with an exposure time of 22 s, and dithered the telescope position between each frame. This allows a sky background to be constructed by median combining the dithered frames. A standard data reduction was carried out using a custom IDL code. This procedure included bad pixel removal, flat-fielding, and subtraction of the sky background. Frames were then aligned and coadded.

2.6. Time Series RVs

TOI-824 was added as a target in two RV TESS follow-up efforts using the Planet Finder Spectrograph (PFS) on the 6.5 m Magellan Clay telescope (Crane et al. 2006, 2008, 2010) at Las Campanas Observatory and the High-Accuracy Radial velocity Planet Searcher (HARPS) spectrograph (Mayor et al. 2003) on the ESO 3.6 m telescope at La Silla Observatory.

PFS is a custom-designed precision RV echelle spectrometer that, with the exception of the focus, has no moving parts. PFS is embedded in an insulated box where the temperature is maintained at 27°C ± 0.01°C. The wavelength range extends from 3900 to 6700 Å. In 2018 January, the old PFS CCD (a 4 K × 4 K detector with 15 μ m pixels) was replaced with a next-generation 10 K × 10 K detector with 9 μ m pixels, improving the sampling by 40%. The peak resolution of PFS

⁴⁰ <http://c-munipack.sourceforge.net>

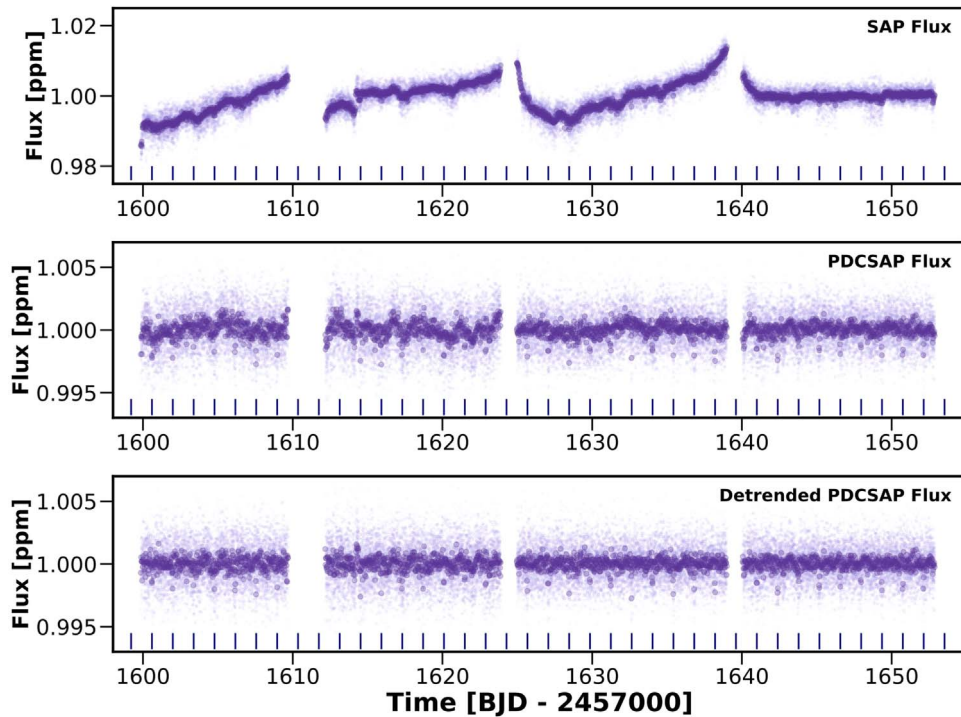


Figure 1. SAP (top), PDCSAP (middle), and detrended PDCSAP (bottom) TESS light curves. The lighter points are the TESS 2 minute cadence flux measurements. The darker points are the same data binned over 30 minutes. The dark blue line segments at the bottom of each panel represent the locations of the transit events identified in the TESS Data Validation Report based on the 2 minute cadence data.

when using the $0''.3$ slit, as was done for all observations of TOI-824, is $R \simeq 130,000$. An iodine cell placed in the converging beam of the telescope is used to provide a precise wavelength metric for velocity measurements (Marcy & Butler 1992). The gaseous iodine blankets the region from 5000 to 6200 Å with a dense forest of sharp absorption lines. The PFS iodine cell was scanned with the NIST FTS spectrometer (Nave 2017) at a resolution of 1 million. The raw data is reduced to 1D spectra with a custom-built raw reduction package. Velocities were generated from an updated version of the iodine modeling package outlined in Butler et al. (1996), and the BJD time stamps were computed using the PEXO software package (Feng et al. 2019).

In contrast, the HARPS spectrograph makes use of multiple observing fibers, one of which is placed on the stellar target while the other is fed by a Fabry–Perot interferometer for a simultaneous wavelength reference. HARPS produces spectra from 3800 to 6900 Å, the entirety of which can be used to measure a star’s RV shift, and has a peak resolving power of $R \simeq 115,000$ (Pepe et al. 2002). Once an observation is complete, a 2D spectrum is optimally extracted from the resulting FITS file. The spectrum is cross-correlated with a numerical mask corresponding to the appropriate spectral type (F0, G2, K0, K5, or M4; we used the G2, which has undergone the most development during the HARPS observing span), and the resulting cross-correlation function is fit with a Gaussian curve to produce an RV measurement (Baranne et al. 1996; Pepe et al. 2002) and calibrated to determine the RV photon-noise uncertainty σ_{RV} .

A total of 24 PFS radial observations were obtained in 2019 July and August, binned into 12 velocity measurements, with a mean internal uncertainty of 0.94 m s^{-1} . A total of eight HARPS observations, binned into five velocity measurements,

Table 2
Binned RV Data of TOI-824

Date (BJD)	RV (m s^{-1})	σ_{RV} (m s^{-1})	Instrument
2458674.64056	4.73	1.91	HARPS
2458675.67088	22.39	2.57	HARPS
2458676.56075	4.42	0.94	PFS
2458677.54783	−11.54	0.92	PFS
2458679.57467	15.06	0.83	PFS
2458680.55934	−3.35	0.79	PFS
2458681.56315	−4.86	1.07	PFS
2458682.54917	12.28	0.84	PFS
2458684.64071	6.30	2.12	HARPS
2458685.53003	11.15	1.03	PFS
2458689.59665	24.17	2.31	HARPS
2458690.61645	18.20	2.30	HARPS
2458703.54142	7.28	0.97	PFS
2458705.51575	−11.65	0.98	PFS
2458708.49699	−4.44	0.73	PFS
2458712.49177	−16.84	1.18	PFS
2458714.48836	14.16	1.03	PFS

were obtained in 2019 July, with a mean internal uncertainty of 2.24 m s^{-1} (Table 2).

3. Analysis

3.1. Transit Detection

Sixteen transits of TOI-824 b were detected in both the MIT Quick Look Pipeline (QLP), which searches for evidence of planet candidates in the TESS 30 minute cadence full-frame images, and in the SPOC pipeline, which analyzes the 2 minute cadence data that TESS obtains for preselected target stars (Jenkins et al. 2016). Initial analyses of the TESS QLP results

found a transit signal with a period of 1.393 days, a depth of ~ 1900 ppm, a duration of 1.3 hr, and the classic flat-bottomed trough shape that is characteristic of a planetary transit. These transit parameters translated to a planet with radius $R_p = 3.4 R_\oplus$ when using the stellar parameters for TOI-824 listed in the eighth installment of the TESS Input Catalog (TIC; Stassun et al. 2019).

Although the measured transit depth and flat-bottomed shape were positive indicators of a transit signal being planetary in nature, the TESS vetting process is designed to guard against a variety of false positives that can mimic this combination. The primary sources of false positives in the TESS data are eclipsing binaries, whether in the form of transiting stars on grazing orbits or as background blends that reduce the amplitude of foreground transit signals, causing them to be deceptively small (e.g., Cameron 2012). Thus, during the TESS vetting process, we carefully inspected the star’s Data Validation Report (DVR; Twicken et al. 2018; Li et al. 2019), which is based on the SPOC 2 minute cadence data for TOI-824. The multisector DVR was found to show no evidence of secondary eclipses, inconsistencies in depth between the even and odd transits, nor correlations between aperture size and transit depth, any of which would be interpreted as a sign of the signal being caused by a nearby eclipsing binary. Additionally, the DVR shows that the location of the transit source is consistent with the position of the target star. After passing these verification steps, the transit signal was assigned the identifier TOI-824.01 and was announced on the MIT TESS data alerts website⁴¹ so that additional follow-up efforts could be coordinated.

3.2. Confirming the Source of the Transit Detection

TESS has large $\sim 21''$ pixels and $\sim 1'$ stellar FWHM, resulting in photometric apertures that typically extend $\sim 1'$ from the central target star location. The large apertures are often contaminated with many nearby stars bright enough to produce the TESS detection. We used our higher spatial resolution follow-up time-series images to search for the location of the periodic flux deficits that caused the detection of TOI-824 b in the TESS data. We checked the light curves of all 338 Gaia DR2 stars within $2.5'$ of TOI-824 that are bright enough to have caused the TESS detection and ruled out nearby eclipsing binaries (EBs) as the source. Furthermore, we detected five transits of TOI-824 b in our ground-based data using target star apertures with radii as small as $1''.2$ centered on TOI-824. The nearest Gaia DR2 or TICv8 star to TOI-824 at the epoch of our follow-up observations is $7''.7$ west. Thus, most of the flux from known nearby stars is excluded from even our larger $4''.7$ target star apertures. We therefore confirm that the source of the flux deficit that is responsible for the TESS detection occurs within a $1''.2$ radius of TOI-824. Our multiband light curves in B , R_c , and Pan-STARRS z bands show that the transits have depths that are consistent across optical wavelengths and with the deblended depth in the TESS data. This rules out certain classes of bound or background EBs that could be blended in the small follow-up photometric apertures as potential sources of the transit detections. Blended EBs that have primary and secondary stars with significantly different effective temperatures are ruled out, while those with

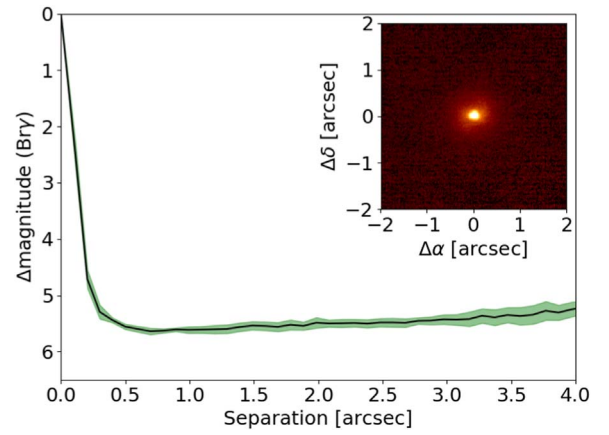


Figure 2. VLT/NaCo contrast curve and image (inset) for TOI-824. Images were taken with a $B_{r\gamma}$ filter and reach a contrast limit of 5 mag at 250 mas. No visual companions are detected anywhere in the field of view.

similar effective temperatures could still possibly produce the transit signals based on the photometric data alone.

3.3. Stellar Kinematics and Population

Adopting the position, proper motion, parallax, and absolute RV provided by Gaia Collaboration et al. (2018), we compute the barycentric galactic velocity of TOI-824 to be U , V , $W = -0.220 \pm 0.152$, -45.803 ± 0.181 , -33.886 ± 0.140 km s^{-1} , with U measured toward the Galactic center, V in the direction of Galactic rotation, and W toward the North Galactic Pole (ESA 1997). Adopting the local standard of rest (LSR) from Schönrich et al. (2010), we find this velocity translates to U_{LSR} , V_{LSR} , $W_{\text{LSR}} = 10.9$, -33.6 , -26.6 km s^{-1} . Using the velocity ellipsoids and population normalizations from Bensby et al. (2003), we estimate the probabilities of kinematic membership of TOI-824 to the thin disk, thick disk, and halo to be 83.9%, 16%, and 0.1%, respectively. Hence, TOI-824 is kinematically most consistent with being a thin disk star. The kinematic parameters corroborate the chemical abundance information provided by TOI-824’s color–magnitude diagram position (in the middle of the main sequence for field stars) and near-solar spectroscopic metallicity ($[\text{Fe}/\text{H}] \simeq -0.1$), suggesting that TOI-824 is a typical thin disk star.

3.4. Stellar Multiplicity

The combined NaCo images show that no additional candidates were detected within the field of view, and that TOI-824 appears single to the limit of our resolution and contrast. The sensitivity of our observations was calculated as a function of radius by injecting fake companions and scaling their brightness until they could be detected with 5σ confidence. The contrast sensitivity is 5 mag at 250 mas and 5.5 mag in the wide field. The contrast sensitivity as a function of radius and a high-resolution image of the star are shown in Figure 2. The lack of companions strongly suggests that the transit signal originates from a planetary companion to TOI-824 b, rather than a background EB, and that the measured radius is not being diluted by a stellar companion (Ciardi et al. 2015).

We also searched for wide companions sharing a similar proper motion and parallax in the Gaia DR2 astrometric catalog (Gaia Collaboration et al. 2018). Any bound companions would likely be seen at separations smaller than the star’s tidal

⁴¹ <http://tess.mit.edu/alerts>

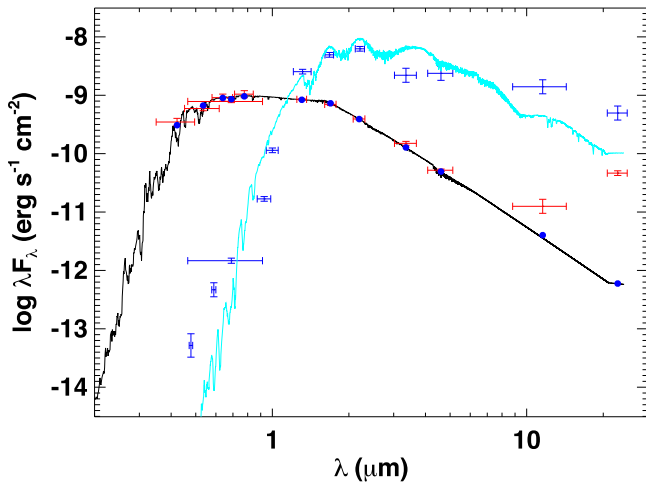


Figure 3. Best-fit SED for TOI-824. Red symbols represent the observed photometric measurements, where the horizontal bars represent the effective width of the passband. Blue symbols are the model fluxes from the best-fit NextGen atmosphere model, which is shown in black. A fit to the infrared-bright source separated by $25''$ is represented by dark blue symbols and a cyan model. Note that the W3 and W4 bands (the two reddest) for TOI-824 were not used in the SED fitting, and the companion was ignored.

(Jacobi) radius ($r_t \simeq 1.35 \text{ pc } (M_*/M_\odot)^{1/3}$), which for the star’s mass of $0.72 M_\odot$ should correspond to about 1.21 pc (Jiang & Tremaine 2010; Mamajek et al. 2013), or $1^\circ 09$ at the Gaia DR2 distance. A search of the Gaia DR2 catalog for stars with parallaxes within 25% of that of TOI-824 within $2r_t$ ($2^\circ 18$) yielded 234 stars. Within a projected separation of one tidal radius ($1^\circ 09$, 1.21 pc), none had a proper motion within 60 mas yr^{-1} ($\Delta v_{\text{tan}} \simeq 18 \text{ km s}^{-1}$) of that of TOI-824. Within two tidal radii, no Gaia DR2 stars had proper motion within 20 mas yr^{-1} ($\Delta v_{\text{tan}} \simeq 6.1 \text{ km s}^{-1}$) of TOI-824. Additionally, among stars within two tidal radii, no other Gaia DR2 candidates lacking parallaxes were found with proper motions within $\pm 20 \text{ mas yr}^{-1}$ of that of TOI-824.

The Gaia DR2 data for entries in the vicinity of TOI-824 are reasonably complete with both parallaxes and proper motions down to $G \simeq 20.0$ ($M_G = 16.0$), and with increasing incompleteness down to $G \simeq 21.4$. Among nearby stars within 25 pc , the absolute magnitude $M_G \simeq 16$ compares well to the M8.5V star 2MASS J11240487 + 3808054 ($M_G = 15.96$, $M_{K_s} = 18.47$; Cruz et al. 2003; Cutri et al. 2003; Gaia Collaboration et al. 2018), whose M_{K_s} value corresponds to mass $0.08 M_\odot$ (Mann et al. 2019), just above the H-burning limit. So our search of the Gaia DR2 catalog for wide companions is likely complete to just above the H-burning limit or $\sim 0.08 M_\odot$.

When we combine our high-contrast imaging data, RV data, and analysis of the Gaia DR2 astrometry for stars in TOI-824’s vicinity, thus far the star appears to be a single star, although objects straddling the H-burning limit or brown dwarfs on wide orbits can not yet be ruled out.

3.5. Spectral Energy Distribution

We performed an analysis of the broadband spectral energy distribution (SED) together with the Gaia DR2 parallax in order to determine an empirical measurement of the stellar radius, following the procedures described in Stassun & Torres (2016) and Stassun et al. (2017, 2018). Together, the available photometry described in Section 2 and Table 1 spans the full stellar SED over the wavelength range $0.4\text{--}22 \mu\text{m}$ (see Figure 3). Noting the large

excess in the WISE3 and WISE4 bands due to a nearby infrared-bright star (IRAS 14448–5722, TIC 1133968082, $T_{\text{mag}} = 19.72$), we chose to exclude them from the fit.

We performed the fit using NextGen stellar atmosphere models, with priors set on the star’s effective temperature (T_{eff}), surface gravity ($\log g$), and metallicity ($[\text{Fe}/\text{H}]$) drawn from the TIC-8. We set the extinction (A_V) to zero due to the proximity of the star, which is consistent with the $A_V = 0.025 \pm 0.06$ value from Lallement et al. (2018). The resulting fit is very good (Figure 3) with a reduced χ^2 of 2.3 and best-fit $T_{\text{eff}} = 4450 \pm 100 \text{ K}$. Integrating the model SED gives the bolometric flux at Earth of $F_{\text{bol}} = (1.442 \pm 0.034) \times 10^{-9} \text{ erg s cm}^{-2}$. Taking the F_{bol} and T_{eff} together with the Gaia parallax, adjusted by $+0.082 \text{ mas}$ to account for the systematic offset reported by Stassun & Torres (2018), gives the stellar radius as $R_* = 0.719 \pm 0.033 R_\odot$, which is consistent with the updated stellar parameters listed in TIC-8.

In order to better estimate the potential flux contamination of the nearby infrared-bright star $\sim 25''$ (~ 1 TESS pixel) from TOI-824, we also performed an SED fit to that source. In this case we also fit for A_V , which we limited to the maximum line-of-sight extinction from the Schlegel et al. (1998) dust maps. We used Gaia G , 2MASS JHK_s , WISE W1–W4, and BV magnitudes from the SPM4.0 catalog (Girard et al. 2011) and z y photometry from the VISTA catalog (Cross et al. 2012). We obtained a best-fit $T_{\text{eff}} = 2750 \pm 250 \text{ K}$ and $A_V = 5.8 \pm 1.9$. The Gaia DR2 parallax for this star is negative, so we instead used the Bayesian distance estimator from Bailer-Jones et al. (2018), which together with the integrated F_{bol} gives an estimated stellar radius of $R_* = 1100 \pm 200 R_\odot$. The infrared-bright source is evidently a distant, highly extinguished red supergiant. We find that the brightness ratio between TOI-824 and this faint supergiant is ~ 7000 in the TESS bandpass, and therefore we conclude that it is unable to affect our measurement of the planet’s radius at a detectable level given the final radius error bars of $\pm 0.1 R_\oplus$.

3.6. Stellar Parameters

We matched the CHIRON spectra against a library of $\sim 10,000$ observed spectra classified by the Stellar Parameter Classification (SPC) pipeline (Buchhave et al. 2012), interpolated via a gradient-boosting regressor. From this analysis, we find the effective temperature, metallicity, surface gravity, and rotational velocity of TOI-824 to be $T_{\text{eff}} = 4665 \pm 100 \text{ K}$, $\log g = 4.68 \pm 0.10 \text{ dex}$, $[\text{m}/\text{H}] = -0.28 \pm 0.10 \text{ dex}$, and $v \sin i = 4.5 \pm 0.5 \text{ km s}^{-1}$, all of which suggested that TOI-824 was suitable for precision radial velocity follow-up efforts.

To determine more precise constraints of the stellar parameters for TOI-824, which have a large influence on the derived planetary parameters, we took one of the spectra from HARPS (which is higher resolution than the spectra provided by CHIRON) and analyzed it using the SPC pipeline described above. From the HARPS spectrum, SPC reports that the star has an effective temperature $T_{\text{eff}} = 4569 \pm 50 \text{ K}$, a surface gravity of $\log(g) = 4.56 \pm 0.10$, and a metallicity of $[\text{m}/\text{H}] = -0.12 \pm 0.08$. We performed a secondary check by running the same HARPS spectra through the SpecMatch-emp software package (Yee et al. 2017), which reported similar results that produced minimal changes when used to derive planetary parameters for TOI-824 b. Given this general agreement, we adopt the HARPS + SPC stellar parameters as the priors for our final EXOFASTv2 analysis of the combined data sets.

Table 3
SPECIES Results for TOI-824

Parameter	Value	Uncertainty
[Fe/H] (dex)	-0.15	0.02
T_{eff} (K)	4616	51
$\log g$ (cm s^{-2})	4.613	0.12
v_r (km s^{-1})	0.188	0.10
$v \sin i$ (km s^{-1})	2.165	0.21
v_{mac} (km s^{-1})	1.542	0.02
No. Fe I lines	131	
No. Fe II lines	8	

Element	Value	Number of Lines
[Na/H]	0.08 ± 0.20	1
[Mg/H]	-0.23 ± 0.12	3
[Al/H]	-0.18 ± 0.12	3
[Si/H]	-0.18 ± 0.12	3
[Ca/H]	-0.48 ± 0.08	7
[Ti I/H]	0.00 ± 0.08	6
[Ti II/H]	0.27 ± 0.14	2
[Cr/H]	-0.12 ± 0.06	12
[Mn/H]	0.03 ± 0.09	5
[Ni/H]	-0.04 ± 0.09	5
[Cu/H]	0.39 ± 0.12	3
[Fe I/H]	-0.07 ± 0.06	13
[Fe II/H]	-0.02 ± 0.10	4

Parameter	Value	54% Confidence Level
Mass (M_{\odot})	0.69	$\begin{matrix} 0.009 \\ 0.007 \end{matrix}$
Age (Gyr)	10.9	$\begin{matrix} 1.8 \\ 3.1 \end{matrix}$
$\log g_{\text{iso}}$ (cm s^{-1})	4.612	$\begin{matrix} 0.011 \\ 0.007 \end{matrix}$
Radius (R_{\odot})	0.68	0.005
$\log(L/L_{\odot})$	-0.72	$\begin{matrix} 0.009 \\ 0.012 \end{matrix}$

3.7. Individual Stellar Abundances

To determine the abundances of specific elements in TOI-824, we combined the individual HARPS spectra into a single, high signal-to-noise ratio (S/N) spectrum and applied the SPECIES code (Soto & Jenkins 2018). SPECIES computes the atmospheric parameters (T_{eff} , $\log g$, [Fe/H], v_r) by measuring the equivalent widths (EWs)⁴² for a set of iron lines. These, together with an ATLAS9 model atmosphere (Castelli & Kurucz 2004), are used to solve the radiative transfer equation in the atmosphere of the star using MOOG (Snedden 1973). Abundances for individual ions are estimated by computing the EWs for a set of lines and using the derived parameters from before to create an appropriate atmospheric model to input to MOOG. Physical parameters, including stellar mass and radius, were obtained by interpolating through a grid of MIST models (Dotter 2016), using the isochrones Python module (Morton 2015). The atmospheric parameters, along with the magnitude of the star at different filters and its parallax (Table 1), were used as priors for the interpolation. Finally, the macroturbulence velocity was obtained from the effective temperature, and the projected rotational velocity by broadening the profiles of a set of absorption lines. The lines used in the fitting procedure, along with the absorption lines used in the abundance determination, are listed in Soto & Jenkins (2018). The results from SPECIES are shown in Table 3.

⁴² The EWs were computed using the EWComputation module available at <https://github.com/msotov/EWComputation>.

3.7.1. Upper Age Constraint from $[\alpha/\text{Fe}]$

Based on the measured abundances of the α elements Mg, Si, Ca, Ti (using only Ti I) and the Fe abundance, we calculate the α enrichment $[\alpha/\text{Fe}]$. We follow Bovy et al. (2016) and calculate a mean α abundance using Mg, Si, Ca, and Ti I, but we omit O and S, which were not measured. Weighting by the number of lines used for the abundance of each species, we estimate $[\alpha/\text{H}] = -0.19$. Given the star's iron abundance $[\text{Fe}/\text{H}] = -0.15 \pm 0.018$, this translates to $[\alpha/\text{Fe}] \simeq -0.04$. From comparison of the $[\text{Fe}/\text{H}]$ and $[\alpha/\text{Fe}]$ estimates to those of local age-dated FGK stars in the survey of Haywood et al. (2013), it appears that stars with TOI-824's metallicity and solar α abundances are all thin disk stars with isochronal ages of $\lesssim 8$ Gyr. While there are older stars with ages ~ 8 –10 Gyr classified as thin disks, they tend to be more metal-poor and more α -rich (Haywood et al. 2013). The kinematic data also support classification of TOI-824 as a likely thin disk star, and its membership as a thin disk provides an independent age constraint (95%CL upper limit) of < 8 Gyr.

3.7.2. Lower Age Constraint from the Li 6707 Å Line

Analysis of the lithium 6707.8 Å line region in the HARPS spectra shows no signs of the absorption feature. We are able to place a strong 10 mÅ upper limit on the line's EW, indicating that TOI-824 is a Li-poor K dwarf. For $T_{\text{eff}} \simeq 4600$ K, a Li 6707 EW < 10 mÅ is inconsistent with (i.e., older than) M7/NGC 6475 (age = 220 Myr, Sestito et al. 2003) and M34 (age = 250 Myr, Jones et al. 1997). That Li EW is consistent with the mixture of detections and nondetections of Li 6707 in the Hyades (age = 700 Myr, Barrado y Navascues & Stauffer 1996) and the Praesepe Cluster (age 590–790 Myr, Cummings et al. 2017). These comparisons show that TOI-824 is almost certainly older than 250 Myr and likely older than 500 Myr.

3.8. System Parameters from EXOFASTv2

To fully characterize the TOI-824 system, we used the EXOFASTv2 software package (Eastman 2017; Eastman et al. 2019) to perform a simultaneous fit to the TESS photometry, the ground-based SG1 photometry, and the RVs from PFS and HARPS. The detrending of the ground-based photometry, to correct for observational effects such as changes in the star's air mass throughout the transit, is handled within EXOFASTv2 using parameters provided by the AIJ software.

3.8.1. EXOFASTv2 Priors and Starting Values

We enforced Gaussian priors on the star's effective temperature ($T_{\text{eff}} = 4569 \pm 114$ K) and metallicity ($[\text{Fe}/\text{H}] = -0.12 \pm 0.08$) using the SPC analysis results of the HARPS spectrum described in Section 3.6, and on the stellar radius ($R_{\star} = 0.719 \pm 0.0333 R_{\odot}$) using the results of the SED fit described in Section 3.5. We also placed a Gaussian prior on the star's parallax from Gaia's DR2 results ($\pi = 15.696178 \pm 0.04934$ mas) after applying the correction from Stassun & Torres (2018). All starting values were further refined using the results of earlier, shorter EXOFASTv2 fits.

The orbit of planet b was defined to be circular in our analysis, as initial EXOFASTv2 fits to the data found eccentricity values consistent with zero and previous studies of small, short-period planets have generally found low eccentricities (Van Eylen & Albrecht 2015; Hadden & Lithwick 2017). We also allowed for

a linear slope to be applied to the RV data during the fitting process. The EXOFASTv2 RV model fits for velocity offsets between the PFS and HARPS data sets as well as different instrumental jitter values, terms that are added in quadrature to the estimated measurement uncertainties from PFS and HARPS to account for systematic effects. To constrain the star’s age, we use EXOFASTv2’s implementation of the MESA Isochrones and Stellar Tracks (MIST) stellar evolution models (Paxton et al. 2013, 2015; Choi et al. 2016; Dotter 2016).

We also fit a dilution term to the TESS photometry to check whether additional correction is needed to address blending from nearby stars. The dilution factor of the TESS photometry is determined by comparing the TESS transit depth to the transit depth measured in the ground-based light curves. The ground-based photometric data has higher spatial resolution, so we expect these transits to experience less flux contamination. We performed two instances of the EXOFASTv2 fit. In the first, which is the version that we use for the final planet parameters presented in Table 4, the TESS dilution parameter is unconstrained. In the second, we enforce a Gaussian prior of 0.0 ± 0.03 on the TESS dilution. If the SPOC pipeline that produced the TESS light curves corrected the blending effects properly, then the best fit to the dilution parameter should be close to zero, regardless of fitting priors.

3.8.2. EXOFASTv2 Results

The median EXOFASTv2 parameters for the TOI-824 system are shown in Table 4, and the best fits to the TESS photometry and PFS and HARPS RV data are shown in Figure 4. The mass of TOI-824 b is measured to be $18.47 \pm 1.84 M_{\oplus}$, which, when combined with the measured planet radius of $2.93 \pm 0.20 R_{\oplus}$, results in a bulk density of $4.03^{+0.98}_{-0.78} \text{ g cm}^{-3}$, making the planet more than twice as dense as Neptune (Figure 5). This radius measurement is roughly 15% smaller than the $R = 3.4 R_{\oplus}$ estimate based on the TESS data alone (Section 3.1), and we address this difference in Section 4. We find that our assumption of a circular orbit is further supported by the fact that the tidal circularization timescale ($\tau_{\text{circ}} \sim 0.57 \text{ Gyr}$) is short compared to the star’s age ($7.5^{+1.8}_{-2.9} \text{ Gyr}$).

For the sake of completeness, we check the S-index and H-index activity indicators extracted from the PFS data set for periodicities that could cause the 1.39 day signal. These activity indicators serve as proxies for chromospheric activity in the visible stellar hemisphere at the moments when the spectra were obtained. The S-index is calculated by measuring the emission reversal at the cores of the Fraunhofer H and K lines of Ca II located at 3968 Å and 3934 Å, respectively (Duncan et al. 1991), while the H-index quantifies the amount of flux within the H α Balmer line core compared to the local continuum. Details on the prescription used to measure these indicators in the PFS data set can be found in Butler et al. (2017). We analyze the resulting S- and H-index values by computing Lomb–Scargle periodograms for each of the activity indicators as well as for the PFS RV values and then looking for any well-defined peaks with false-alarm probabilities $< 0.1\%$ in the vicinity of the planet’s period (Figure 6).

The RV signal of TOI-824 b is apparent in the Lomb–Scargle periodogram of the PFS RVs (Figure 6). Neither the S- nor H-index periodogram displays any significant peaks at periods close to the planetary signal, however, which means stellar activity is unlikely to skew or otherwise influence our

measurement of the planet’s mass. Indeed, based upon these periodograms, TOI-824 appears to be a relatively quiet star.

Given the match in both period and phase between the TESS signal and the planet signal seen in the combined RV data set, along with the lack of any significant periodicity in the spectral activity indicators, we consider this to be a decisive confirmation of the planetary nature of TOI-824 b.

4. Correction to TESS Background Flux Estimates

The final EXOFASTv2 fit finds a significant, negative dilution factor ($A_D = -0.26$) for the TESS photometry. This dilution value is determined by comparing the $\sim 1888 \text{ ppm}$ depth of the TESS transits to the 1490 ppm depth of the ground-based transits, and a negative A_D value indicates that the TESS light curve has a higher out-of-transit flux than is reported by the SPOC pipeline. The TESS SPOC data therefore exhibit larger fractional flux drops during transit events, leading to a larger measured planet radius. In the case of TOI-824 b, including the TESS dilution value in the EXOFASTv2 fit results in a 13% decrease in the measured planet radius when compared to earlier fits that used only the TESS data to measure R_p and not the ground-based follow-up data.

We first investigated whether this offset could be caused by an inaccurate correction in the TESS data for the effects of nearby stars, as TOI-824 is in a crowded part of the sky and numerous additional sources fall within the SPOC aperture. We find, however, that this is not the case. The TESS SPOC pipeline includes a crowding correction to address the effects of flux from nearby sources. This correction is based on a simulated star scene for each CCD that is created using the detectors’ pixel response functions (measured during commissioning) and stars in the TIC catalog that are imaged by the CCD. The simulated star scene is used to estimate the fraction of flux within a given TOI’s photometric aperture that is due to the target star compared to the total flux contributed by all stars whose images fall within the photometric aperture. That ratio is then used to correct the resulting SPOC light curve. Like all stars observed in Sectors 1–13, TOI-824’s crowding correction is based on TICv7, which uses the Gaia DR1 and 2MASS catalogs, among others. The more recent TICv8, however, is based on the Gaia DR2 catalog and identifies an additional 1049 stars within that same radius (Figure 7). While this is a large increase in nearby stellar neighbors, 99.6% of the newly identified TICv8 stars are fainter than $T_{\text{mag}} = 15$ (five TESS magnitudes fainter than TOI-824) and 91% are fainter than $T_{\text{mag}} = 18$. But accounting for these additional faint TICv8 stars, present in the TESS images but not included in the crowding correction, would increase the deblended SPOC depth and resulting planet radius rather than decrease it, exacerbating the issue.

The discrepancy comes instead from an overestimation of the TESS background flux caused by the plethora of nearby stars, many of which fall into TOI-824’s postage stamp aperture (Figure 8). When examining the pixels that make up the Sector 11 postage stamp for TOI-824, we find that the dimmest background-corrected pixels have a median value of roughly $-180 \text{ e}^-/\text{s}$. This suggests that the background level measured in the postage stamp’s “empty” pixels—which, given the high stellar density of the region, are not truly empty—was too high, and its subtraction from the TOI-824 aperture produced negative flux measurements in some pixels. If we adjust the mean flux of the postage stamp upward by $8 \times 180 \text{ e}^-/\text{s}$ to

Table 4
Median Values and 68% Confidence Interval for EXOFASTv2 Results on TOI-824

Parameter	Units	Values	
EXOFASTv2 Gaussian Priors:			
R_*	Stellar radius (R_\odot)	0.719 ± 0.033	
T_{eff}	Effective temperature (K)	4569 ± 114	
[Fe/H]	Metallicity (dex)	-0.12 ± 0.080	
ϖ	Parallax (mas)	15.696178 ± 0.04934	
A_v	V-band extinction (mag)	0.025 ± 0.06	
EXOFASTv2 Hard Bounds on Parameters:			
$\log g$	Surface gravity (cgs)	[3, 5]	
Age	Age (Gyr)	[0, 10]	
T_{eff}	Effective temperature (K)	[4000, 8000]	
[Fe/H]	Metallicity (dex)	[-1, 0.5]	
Stellar Parameters:			
M_*	Mass (M_\odot)	$0.710^{+0.032}_{-0.031}$	
R_*	Radius (R_\odot)	0.695 ± 0.027	
L_*	Luminosity (L_\odot)	$0.195^{+0.028}_{-0.025}$	
ρ_*	Density (cgs)	$2.98^{+0.30}_{-0.27}$	
$\log g$	Surface gravity (cgs)	4.605 ± 0.026	
T_{eff}	Effective temperature (K)	4600^{+110}_{-100}	
[Fe/H]	Metallicity (dex)	$-0.092^{+0.076}_{-0.077}$	
[Fe/H] ₀	Initial metallicity	$-0.080^{+0.077}_{-0.079}$	
Age	Age (Gyr)	$7.5^{+1.8}_{-2.9}$	
EEP	Equal evolutionary phase	$333.7^{+7.1}_{-13}$	
$\dot{\gamma}$	RV slope ($\text{m s}^{-1} \text{ day}^{-1}$)	-0.138 ± 0.067	
A_D	TESS dilution from neighboring stars	$-0.26^{+0.11}_{-0.13}$	
Planetary Parameters:			
P	Period (days)	$1.392978^{+0.000018}_{-0.000017}$	
R_p	Radius (R_E)	$2.926^{+0.202}_{-0.191}$	
M_p	Mass (M_E)	$18.467^{+1.843}_{-1.875}$	
T_C	Time of conjunction (BJD _{TDB})	$2458597.81419^{+0.00063}_{-0.00065}$	
T_0	Optimal conjunction time (BJD _{TDB})	$2458639.60354 \pm 0.00035$	
a	Semimajor axis (au)	0.02177 ± 0.00032	
i	Inclination (degrees)	$83.65^{+0.39}_{-0.38}$	
T_{eq}	Equilibrium temperature (K)	1253^{+38}_{-37}	
τ_{circ}	Tidal circularization timescale (Gyr)	$0.57^{+0.23}_{-0.16}$	
K	RV semi-amplitude (m s^{-1})	$13.2^{+1.2}_{-1.3}$	
$\log K$	Log of RV semi-amplitude	$1.121^{+0.039}_{-0.044}$	
R_p/R_*	Radius of planet in stellar radii	$0.0387^{+0.0018}_{-0.0019}$	
a/R_*	Semimajor axis in stellar radii	$6.73^{+0.22}_{-0.21}$	
δ	Transit depth (fraction)	0.00149 ± 0.00014	
Depth	Flux decrement at midtransit	0.00149 ± 0.00014	
τ	Ingress/egress transit duration (days)	$0.00386^{+0.00037}_{-0.00034}$	
T_{14}	Total transit duration (days)	$0.04806^{+0.00081}_{-0.00080}$	
T_{FWHM}	FWHM transit duration (days)	$0.04419^{+0.00084}_{-0.00085}$	
b	Transit impact parameter	$0.745^{+0.022}_{-0.024}$	
$\delta_{S,3.6 \mu\text{m}}$	Blackbody eclipse depth at $3.6 \mu\text{m}$ (ppm)	86^{+12}_{-11}	
$\delta_{S,4.5 \mu\text{m}}$	Blackbody eclipse depth at $4.5 \mu\text{m}$ (ppm)	126^{+16}_{-15}	
ρ_p	Density (cgs)	$4.03^{+0.98}_{-0.78}$	
$\log g_p$	Surface gravity	$3.323^{+0.069}_{-0.070}$	
Θ	Safronov number	0.0136 ± 0.0016	
$\langle F \rangle$	Incident flux ($10^9 \text{ erg s}^{-1} \text{ cm}^{-2}$)	$0.561^{+0.070}_{-0.063}$	
T_p	Time of periastron (BJD _{TDB})	$2458597.81419^{+0.00063}_{-0.00065}$	
M_p/M_*	Mass ratio	$0.0000782^{+0.0000074}_{-0.0000076}$	
d/R_*	Separation at midtransit	$6.73^{+0.22}_{-0.21}$	
Telescope Parameters:			
γ_{rel}	Relative RV offset (m s^{-1})	HARPS 12.9 ± 2.4	PFS 1.3 ± 1.0

Table 4
(Continued)

Parameter	Units	Values	
σ_J	RV jitter (m s^{-1})	$4.3^{+3.0}_{-2.1}$	$3.21^{+1.3}_{-0.81}$
σ_J^2	RV jitter variance	18^{+35}_{-14}	$10.3^{+9.6}_{-4.5}$
RMS	rms of RV residuals (m s^{-1})	2.58	2.71

Note. Notes from Eastman et al. (2019): The star’s age is calculated using the MIST isochrones. The optimal conjunction time (T_0) is the time of conjunction that minimizes the covariance with the planet’s period and therefore has the smallest uncertainty. The equilibrium temperature of the planet (T_{eq}) is calculated using Equation (1) of Hansen & Barman (2007) and assumes no albedo and perfect heat redistribution. The tidal circularization timescale (τ_{circ}) is calculated using Equation (3) from Adams & Laughlin (2006) and assumes $Q = 10^6$. The 3.6 and 4.6 μm secondary occultation depths use a blackbody approximation of the stellar flux, F_* , at T_{eff} and of the planetary flux, F_p , at T_{eq} and are calculated using $\delta_{S,\lambda} = \frac{(R_p/R_*)^2}{(R_p/R_*)^2 + (F_*/F_p)}$.

account for the eight pixels in the optimal aperture, then the mean flux becomes 13640 e^-/s . This reduces the SPOC transit depth from 1888 to 1663 ppm for Sector 11, a 12% decrease that produces a 6% reduction in the planetary radius.

The ground-based photometry, however, suggests an even smaller transit depth of 1490 ppm, which is 21% below the original SPOC transit depth and another 10% below the corrected value outlined above. Given that no pixel within the TOI-824 postage stamp is completely devoid of stars, making an accurate estimate of the background flux nigh on impossible, we find it to be very plausible that an additional factor of 10% overestimation could be folded into the SPOC light curves. To investigate this possibility, we examined a 51×51 pixel full-frame cutout image from Sector 11 centered on TOI-824. After examining the star’s full-frame image time series, we selected an image that is minimally contaminated with scattered light, which turned out to be the last full-frame image taken in Sector 11. We identified the darkest 40 pixels in the full-frame image and calculated an average background of 325 e^-/s , which resulted in an adjusted SPOC Sector 11 depth of 1517 ppm. This adjusted depth is now within 2% of the ground-based depth, verifying that it is indeed the background flux estimation causing the TESS pipeline to report an inflated planet radius.

The radius offset between the TESS and SG1 data for TOI-824 b highlights the importance of inspecting TESS data products at the pixel level before using them to determine planet characteristics. And it reinforces even more so the critical role that ground-based follow-up transit observations and fitting approaches that allow for offsets between independent light curves play in correctly measuring planet radii. While this is most relevant when considering stars in crowded regions, as in the case of TOI-824, the general principle holds for almost any exoplanet science derived from TESS data. Similar effects from incorrect background corrections have been seen in both Kostov et al. (2020) and Feinstein et al. (2020). Kostov et al. (2020) corrects the offset by using the TESS full-frame images to infer an appropriate background flux, which then gets added back into the 2 minute cadence data, similar to our approach using the ground-based SG1 photometry. In comparison, Feinstein et al. (2020) determines their background estimate by analyzing a given star’s entire postcard region (148×104 pixels) and then subtracting the resulting background flux before extracting the target pixel files, which are in turn used to produce light curves.

We expect the background subtraction bias seen here to predominantly affect dim stars or stars in highly crowded regions. Indeed, when investigating all 2 minute targets in Sector 14, which included the plane of the galaxy, we find that if all stars

hosted transiting planets, then the change in planet radius due to background bias would be less than 1% for 70% of cases. In Sector 22, which does not include the plane of the galaxy and therefore has less stellar crowding, if we again assume that all targets host transiting planets, then the percentage of planets affected at the <1% level rises to 87%. Thus for most objects of interest, the change in planet radius due to background bias will likely be much smaller than other sources of error in planet radius.

TOI-824, which sits in a very crowded region of the sky, is one of the strongest background bias cases detected to date with a 10.5% planet radius reduction. In response to this issue, the SPOC has updated the background estimation algorithm to prevent background-subtracted pixel time series from being significantly negative and will begin applying it starting with Sector 27. As a general guideline, we recommend that when working with TESS photometry scientists should, whenever possible, incorporate some additional measure of the transit depth into their analysis instead of relying solely on the 2 minute photometry. These additional analysis measures will become especially important when TESS begins its observations of the more crowded ecliptic equator in Cycle 4.

5. Discussion

5.1. Interior Characterization of TOI-824 b

We model the interior of TOI-824 by assuming a pure iron core, a silicate mantle, a pure water layer, and a H–He atmosphere. We follow the structure model of Dorn et al. (2017), with the equation of state (EOS) of the iron core taken from Hakim et al. (2018), the EOS of the silicate mantle calculated using PERPLE_X by Connolly (2009) given thermodynamic data of Stixrude & Lithgow-Bertelloni (2011), and Saumon et al. (1995) for the H–He envelope assuming protosolar composition. For the water, we use the quotidian equation of state presented in Vazan et al. (2013) for low pressures and the tabulated EOS from Seager et al. (2007) for pressures above 44.3 GPa. We then use a generalized Bayesian inference analysis using a nested sampling scheme (e.g., Buchner 2016) to quantify the degeneracy between interior parameters and produce posterior probability distributions. We use the stellar Fe/Si and Mg/Si ratios as a proxy for the planet, and we assume an envelope luminosity of $L = 10^{22.52}$ erg s^{-1} (equal to Neptune’s luminosity).

Table 5 lists the inferred mass fractions of the core, mantle, water layer, and H–He atmosphere from our structure models. We find a median H–He mass fraction of 2.8%, which is a lower bound because enriched H–He atmospheres are more compressed and can therefore increase the planetary H–He mass fraction. Indeed, formation models of mini-Neptunes

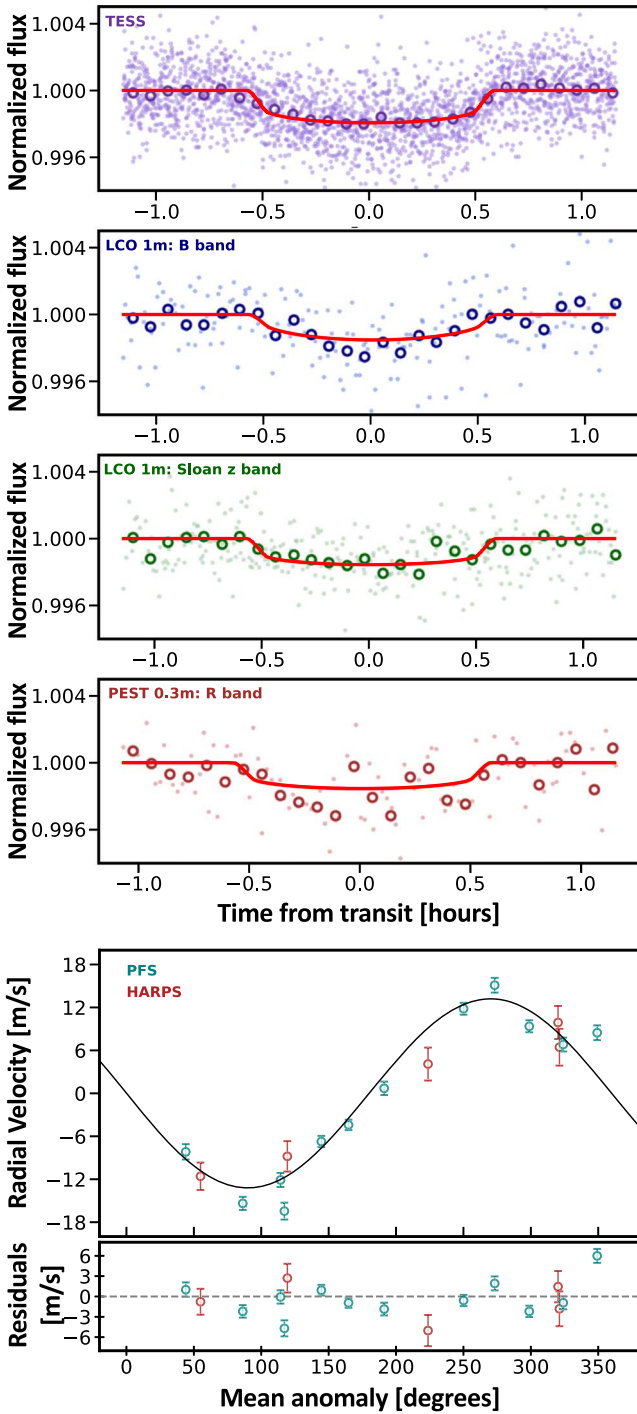


Figure 4. Results of the EXOFASTv2 joint fit to the detrended photometry from TESS, LCO, and PEST (top panels) and the RV measurements from PFS and HARPS (bottom panel). Light points in the photometry panels depict the unbinned observations, while darker circles show the data in 30 minute bins. Solid lines show the best-fit models to both the photometry and RV data sets. The planet’s transit has a depth of 1490 ppm and a total duration of 1.15 hr, while the RV curve has a semiamplitude of 13.2 m s^{-1} .

suggest that it is very unlikely to form such planets without envelope enrichment (Venturini & Helled 2017). The core, mantle, and water layer have relative mass fractions between 27%, 38%, and 31% with large sigma. This regime of the mass–radius relation is very degenerate, and therefore it is not possible to accurately determine the mass ratios of the core, mantle, and water layer.

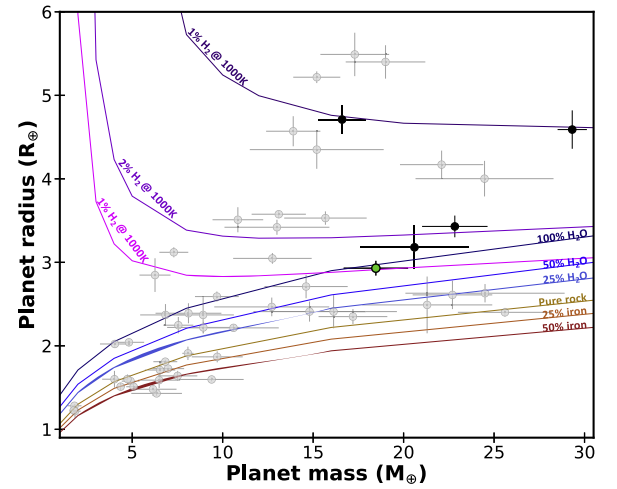


Figure 5. Mass–radius diagram for confirmed planets with masses and radii measured to better than 25% (gray points) retrieved from the Exoplanet Archive (<https://exoplanetarchive.ipac.caltech.edu>). Black points show the other hot Neptune planets recently discovered by TESS and Next-Generation Transit Survey (NGTS). TOI-824 b is denoted with a green circle. Composition curves from Zeng et al. (2016, 2019) are shown as solid colored lines.

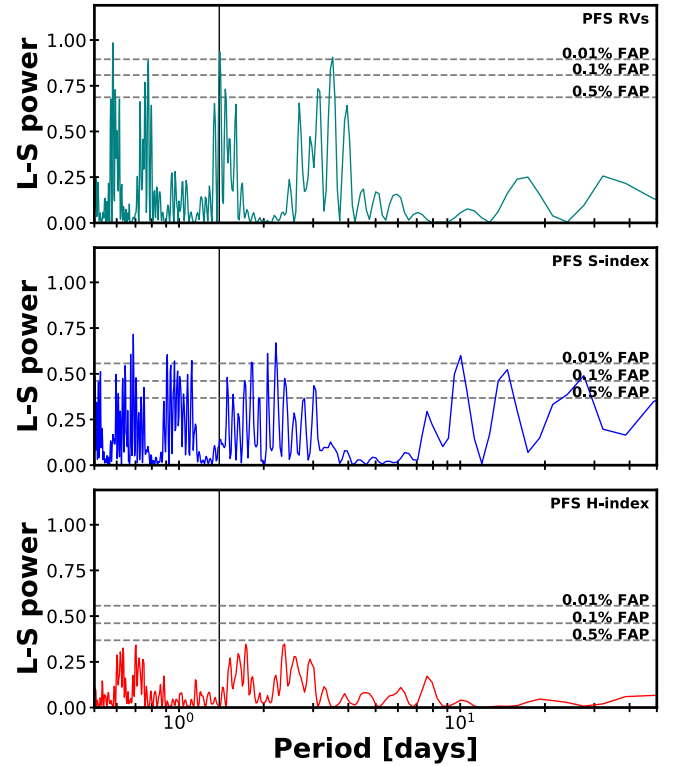


Figure 6. Lomb–Scargle periodograms of the RVs (top), S-index values (middle), and H-index values (bottom) extracted from the PFS spectra. The period of TOI-824 b is marked by a vertical line in each panel, and the 0.5%, 0.1%, and 0.01% false-alarm probabilities are marked with dashed, horizontal lines. The signal of the planet is clearly visible in the top panel, but neither of the activity indicator periodograms display significant peaks in the same region of period space.

5.2. Structure and Atmospheric Evolution of TOI-824 b

One of the most intriguing results of NASA’s Kepler mission is clear evidence that the overall distribution of small, short-period planets has been sculpted by processes that erode atmospheres (e.g., Lopez et al. 2012; Owen & Wu 2013, 2017;

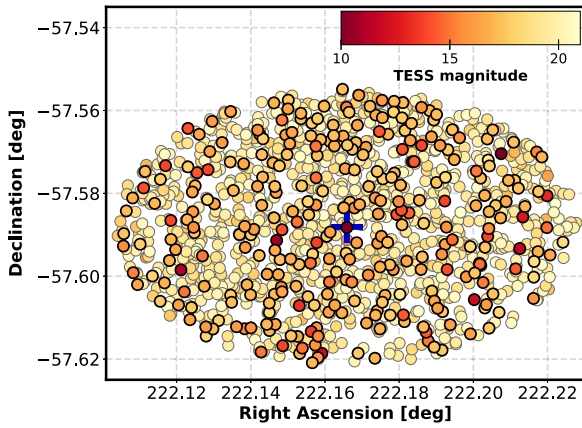


Figure 7. Stars present in TICv7 (black outlines) and TICv8 (gray outlines) within 2' of TOI-824, which is identified with a blue cross. All TICv7 stars are also present in TICv8, along with an additional 1049 stars identified by Gaia DR2. The vast majority of these additional stars are more than 8 TESS magnitudes fainter than TOI-824, so we do not anticipate them causing problems with the crowding correction.

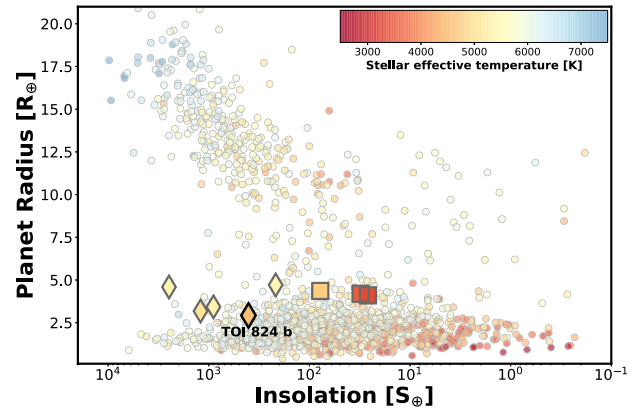


Figure 9. TOI-824 b (black diamond) sits on the lower edge of the hot Neptune desert. Other hot Neptunes discovered within the past year (TOI 132 b, LTT 9779 b, NGTS-4b, and HD 219666 b) are shown as diamonds, while comparable planets with well-studied atmospheres (HAT-P-11b, GJ 3470 b, and GJ 436 b) are shown as squares. TOI-824 b inhabits a notably different region of this parameter space than even the most irradiated of the planets with well-studied atmospheres (HAT-P-11b) and offers an opportunity to investigate how increased irradiation affects a variety of atmospheric characteristics.

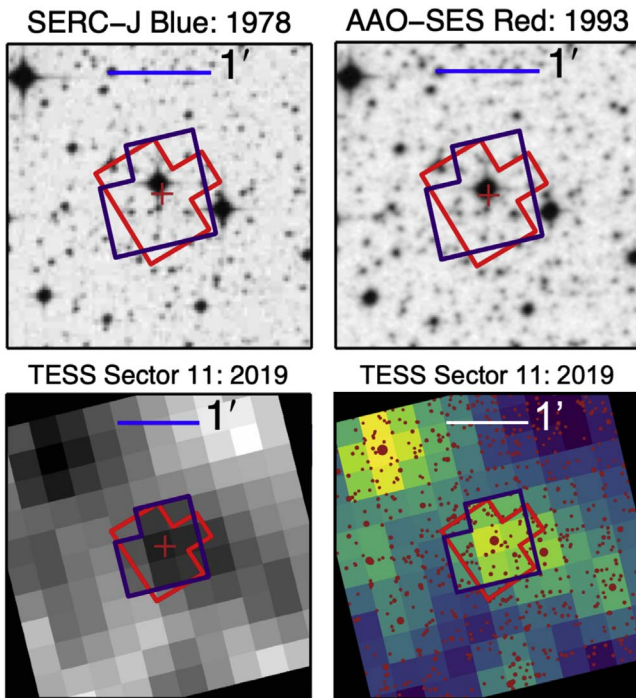


Figure 8. Images of the crowded star field surrounding TOI-824. The red cross in each image is the present-day location of TOI-824, and the purple and red lines mark the boundary of the TESS photometric apertures for Sectors 11 and 12, respectively. North is up and east is to the left in all images. Top left: SERC-J survey, wavelength coverage from the UV to 540 nm. Top right: ESO/SERC Southern Sky Atlas, wavelength coverage 590–690 nm. Bottom left: summed TESS Sector 11 image. Bottom right: single TESS Sector 11 frame with Gaia DR2 sources depicted as maroon circles.

Chen & Rogers 2016; Jin & Mordasini 2018). This evidence includes both the clear gap in the planet radius distribution uncovered by Fulton (2017) and better documented in Fulton et al. (2017) and Fulton & Petigura (2018), as well as the dearth of nonrocky 2–4 R_{\oplus} planets in the most strongly irradiated orbits (e.g., Sanchis-Ojeda et al. 2014; Lundkvist et al. 2016; McDonald et al. 2019), which is frequently referred to as the hot Neptune desert. This desert is normally shown by

Table 5
Inferred Interior Structure Properties of TOI-824 b

$M_{\text{core}}/M_{\text{total}}$	$0.27^{+0.23}_{-0.11}$
$M_{\text{mantle}}/M_{\text{total}}$	$0.38^{+0.25}_{-0.18}$
$M_{\text{water}}/M_{\text{total}}$	$0.31^{+0.24}_{-0.18}$
$M_{\text{atm}}/M_{\text{total}}$	$0.028^{+0.008}_{-0.007}$

examining the distribution of planetary radii and insolation, as in Figure 9, but this is closely related to similar concepts like the “cosmic shoreline” described in Zahnle & Catling (2017), which compares planetary insolation and escape velocity, as well as the mass-loss thresholds found by comparing planetary binding energies to the high ionizing X-ray and EUV irradiation they receive (e.g., Lecavelier Des Etangs 2007; Lopez & Fortney 2013, 2014; Owen & Wu 2013). Indeed, the hot Neptune desert and the radius gap closely match prior predictions from models of extreme atmospheric escape due to XUV-driven photoevaporative escape (e.g., Owen & Jackson 2012; Lopez & Fortney 2013; Owen & Wu 2013; Jin et al. 2014; Lopez 2017), although other extreme escape mechanisms have subsequently been proposed to explain these features (e.g., Schlichting et al. 2015; Ginzburg et al. 2018).

TOI-824 b is particularly interesting in the context of the hot Neptune desert because, along with a handful of other recent discoveries, it appears to lie at the lower edge of the desert (see Figure 9). Its mass and radius, however, indicate that TOI-824 b must possess a significant primary atmosphere. Assuming a rock and iron core, thermal evolution models from Lopez & Fortney (2014) suggest a H+He envelope fraction of $2.4^{+1.1}_{-1.7}\%$, consistent with the findings in Section 5.1. This is well within the typical range of the warmest Neptune planets discovered by Kepler, although of course those are typically much less irradiated than TOI-824 b is. This poses an interesting question: how could this planet have possibly retained a significant gaseous envelope despite receiving extreme radiation?

Planet evolution and escape models may be able to explain this conundrum. Along with other recent discoveries in and around the desert such as K2-100b (Barragán et al. 2019), HD 219666 b (Esposito et al. 2019), NGTS-4 b (West et al. 2019), TOI-132 b

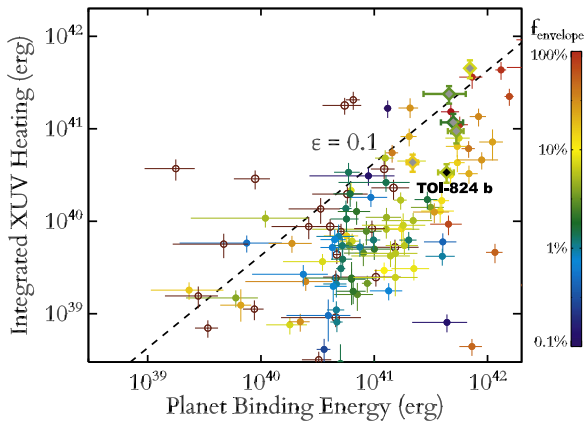


Figure 10. Despite their extremely high irradiances, the recent crop of ultrahot Neptunes found in and near the hot Neptune desert fit into the wider population of known exoplanets when we consider their exceptionally high masses. Updated from Lopez & Fortney (2014), this diagram compares the total XUV heating that a planet’s atmosphere has received over its lifetime to its gravitational binding energy, with planets at the top left being the most vulnerable to extreme atmospheric escape from photoevaporation. Planets are color-coded based on their estimated H+He gas fraction, with likely bare rocky planets shown by open rust-colored points. Previously known planets are depicted as circles, while the six new high-mass hot Neptunes are plotted as diamonds. The dashed line shows a widely used analytic approximation of atmospheric survivability from Lopez et al. (2012) assuming a 10% XUV heating efficiency.

(Díaz et al. 2020), and LTT 9779 b (J. T. Jenkins 2020, private communication), TOI-824 b is exceptionally massive given its radius. All of these planets have masses in excess of $16 M_{\oplus}$ despite the fact that planets in this size range ($3\text{--}5 R_{\oplus}$) are more typically $6\text{--}10 M_{\oplus}$ (Wolfgang et al. 2016; Ning et al. 2018). Such high masses mean that these planets are more resilient to atmospheric escape because a planet’s timescale to lose its atmosphere to photoevaporative escape scales roughly as M_p^{-2} (Lopez & Fortney 2013). Indeed, when viewed in the context of their gravitational binding energy and their XUV irradiation (Figure 10), these new discoveries appear more typical, lying close to but not beyond the limits of potential survival to escape, similar to other previously known hot Neptunes and sub-Neptunes.

Although the large planet mass may help explain how TOI-824 b’s atmosphere survived, the existence of these large planet masses alone poses intriguing questions for theorists. Structure models indicate that most of this large mass is likely in the planet’s heavy element core (Lopez & Fortney 2014). Given its extremely short orbital period, however, we must ask how TOI-824 b and similar planets accumulated such a large amount of heavy elements on such an irradiated orbit in the first place. Theorists have long argued that hot Jupiters likely migrate in from much more distant orbits, but it has been debated whether this is also true of lower mass planets. Studies of ultrashort-period rocky planets and of the overall distribution of Kepler planets indicate that there is likely some mass enhancement in the inner parts of planetary disks compared to the classic minimum mass solar nebula (e.g., Chiang & Laughlin 2013). However, with $\sim 18.6 M_{\oplus}$ and an orbital period of only 1.4 days, systems like TOI-824 may require an even stronger concentration or migration of heavy elements in the inner part of the planetary disk.

5.3. Potential for Atmospheric Characterization

Hot Neptunes are particularly compelling targets for follow-up atmosphere characterization. Their high equilibrium temperatures

make it more likely that their atmospheres are cloud-free (Crossfield & Kreidberg 2017). Their elevated temperatures also mean that they are good targets for thermal emission measurements taken during secondary eclipse, which are less affected by clouds and hazes than transmission spectra (Fortney 2005). The number of Neptune-sized planets in this desired insolation range is currently very limited, however, and only a small number have been studied in depth and had their atmospheres confirmed. Most notable among this population are GJ 436 b (Butler et al. 2004; Morley et al. 2017), GJ 3470 b (Bonfils et al. 2012; Benneke et al. 2019), and HAT-P-11b (Bakos et al. 2010; Fraine et al. 2014), which are denoted by the square points in Figure 9.

TOI-824 b is also a compelling target because its mass is precisely known. Batalha et al. (2019) showed that in order to infer the atmospheric properties of an exoplanet, the planet’s mass must be measured to at least the 20% level. Otherwise the widths of the posterior distributions of the atmospheric properties are dominated by the uncertainties in the planet’s mass.

Absorption features from several key molecular species in the atmosphere of TOI-824 b may be detectable with current ground- and space-based facilities. Hubble/WFC3 observations in the near-infrared could reveal water features, assuming a cloud-free, $100\times$ solar metallicity atmosphere. Molecular features from water and CO may also be accessible with high-resolution ground-based spectrographs such as CRIFES+ at the VLT (Follert et al. 2014). In addition to these molecular species, TOI-824 b is hot enough that alkali metals may be present in the gas phase in the atmosphere, in contrast to previously characterized small planets (Morley et al. 2015). The ESPRESSO spectrograph on VLT (Pepe et al. 2014), for example, should be able to detect sodium in the atmosphere of TOI-824 b. Many additional chemical species will be observable with next-generation facilities like the ELTs that have broader wavelength coverage.

We note that the expected S/N for atmospheric features for TOI-824 b is not the highest for all sub-Neptunes discovered by TESS. It sits just barely above the cutoff suggested by Kempton et al. (2018), at a transmission spectroscopy metric (TSM) of 85 compared to the suggested inclusion criteria of $\text{TSM} \geq 84$, which was designed to yield a statistical sample of planets in this size range that are accessible with a modest amount of James Webb Space Telescope time per planet. That threshold S/N assumes the atmospheres are cloud-free, however, which is not necessarily the case (Crossfield & Kreidberg 2017). If TOI-824 b follows the trend noted in Crossfield & Kreidberg (2017), then it may have relatively large spectral features due to its high temperature. Atmosphere characterization is worth pursuing to test this hypothesis.

TOI-824 b is also a promising target for the detection of atmospheric escape. At the edge of the hot Neptune desert, the planet has likely experienced significant photoevaporation over its lifetime and into the present. Observations of the helium near-IR triplet may reveal atmospheric escape in action and constrain the rate of evaporative mass loss (Salz et al. 2018; Spake et al. 2018; Ninan et al. 2020), and similar studies could be carried out using observations of $\text{H}\alpha$ (Jensen et al. 2012, 2018; Cauley et al. 2017; Yan & Henning 2018) and $\text{Ly}\alpha$ (Ehrenreich et al. 2015; Bourrier et al. 2018). Conveniently, TOI-824 b has a K dwarf host star, which is the optimal stellar spectral type to excite neutral helium atoms (Oklopčić & Hirata 2018; Oklopčić 2019).

As of now, the detectability of TOI-824 b’s atmosphere from both ground and space is promising and could lead to detailed

characterization of the most irradiated small planet at the edge of the desert that has retained its atmosphere to date.

This paper includes data collected by the TESS mission. Funding for the TESS mission is provided by the NASA Explorer Program. We acknowledge the use of public TESS Alert data from pipelines at the TESS Science Office and the TESS Science Operations Center. This paper includes data gathered with the 6.5 m Magellan Telescopes located at Las Campanas Observatory, Chile. This work makes use of observations from the LCOGT network. This study is based on observations collected at the European Southern Observatory under ESO programs 0103.C-0874 (PI Nielsen) and 0103.C-0449(A). This work has made use of data from the European Space Agency (ESA) mission Gaia (<https://www.cosmos.esa.int/gaia>), processed by the Gaia Data Processing and Analysis Consortium (DPAC, <https://www.cosmos.esa.int/web/gaia/dpac/consortium>). Funding for the DPAC has been provided by national institutions, in particular the institutions participating in the Gaia Multilateral Agreement.

Resources supporting this work were provided by the NASA High-End Computing (HEC) Program through the NASA Advanced Supercomputing (NAS) Division at Ames Research Center for the production of the SPOC data products. Some or all of the data presented in this paper were obtained from the Mikulski Archive for Space Telescopes (MAST). Support for MAST for non-HST data is provided by the NASA Office of Space Science via grant NNX13AC07G and by other grants and contracts. This research has made use of the NASA Exoplanet Archive, which is operated by the California Institute of Technology, under contract with the National Aeronautics and Space Administration under the Exoplanet Exploration Program. This research has made use of NASA's Astrophysics Data System. This research has also made use of the Exoplanet Follow-up Observation Program website, which is operated by the California Institute of Technology, under contract with the National Aeronautics and Space Administration under the Exoplanet Exploration Program. This research made use of Astropy, a community-developed core Python package for Astronomy (Astropy Collaboration et al. 2013).


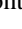
Part of this research was carried out at the Jet Propulsion Laboratory, California Institute of Technology, under a contract with the National Aeronautics and Space Administration (NASA). J.A.B., C.X.H., and M.N.G. acknowledge support from MIT's Kavli Institute as Torres postdoctoral fellows. J.H. acknowledges the support from the Swiss National Science Foundation under grant 200020_172746. J.V.S. is supported by funding from the European Research Council (ERC) under the European Union's Horizon 2020 research and innovation program (project FOUR ACES; grant agreement No. 724427). Support for this work was provided by NASA through Hubble Fellowship grant HST-HF2-51399.001 awarded to J.K.T. by the Space Telescope Science Institute, which is operated by the Association of Universities for Research in Astronomy, Inc., for NASA, under contract NAS5-26555. T.D. acknowledges support from MIT's Kavli Institute as a Kavli postdoctoral fellow. X.D. acknowledges support from the Branco-Weiss Fellowship as well as from the European Research Council (ERC) under the European Union's Horizon 2020 research and innovation program (grant agreement No. 851555) This material is based upon work supported by the National Science Foundation Graduate Research Fellowship Program under grant No. DGE-1746045. Any opinions, findings, and conclusions

or recommendations expressed in this material are those of the author(s) and do not necessarily reflect the views of the National Science Foundation.

Facilities: TESS, Magellan:Clay (Planet Finder Spectrograph), ESO:3.6 m (HARPS), CTIO:1.5 m (CHIRON), VLT:Antu (NACO).

Software: EXOFAST (v2 Eastman 2017; Eastman et al. 2019), Tapir (Jensen 2013), AstroImageJ (Collins et al. 2017), SpecMatch-emp (Yee et al. 2017), astropy (Astropy Collaboration et al. 2013), SPECIES (Soto & Jenkins 2018), isochrones Python module (Morton 2015), MOOG (Snedden 1973; Sneden et al. 2012), PEXO (Feng et al. 2019), EWComputation (<https://github.com/msotov/EWComputation>).

ORCID iDs

Jennifer A. Burt  <https://orcid.org/0000-0002-0040-6815>
 Louise D. Nielsen  <https://orcid.org/0000-0002-5254-2499>
 Samuel N. Quinn  <https://orcid.org/0000-0002-8964-8377>
 Eric E. Mamajek  <https://orcid.org/0000-0003-2008-1488>
 Elisabeth C. Matthews  <https://orcid.org/0000-0003-0593-1560>
 George Zhou  <https://orcid.org/0000-0002-4891-3517>
 Julia V. Seidel  <https://orcid.org/0000-0002-7990-9596>
 Chelsea X. Huang  <https://orcid.org/0000-0003-0918-7484>
 Maritza Soto  <https://orcid.org/0000-0001-9743-5649>
 Keivan G. Stassun  <https://orcid.org/0000-0002-3481-9052>
 Laura Kreidberg  <https://orcid.org/0000-0003-0514-1147>
 Karen A. Collins  <https://orcid.org/0000-0001-6588-9574>
 Jason D. Eastman  <https://orcid.org/0000-0003-3773-5142>
 Joseph E. Rodriguez  <https://orcid.org/0000-0001-8812-0565>
 Andrew Vanderburg  <https://orcid.org/0000-0001-7246-5438>
 Samuel P. Halverson  <https://orcid.org/0000-0003-1312-9391>
 Sharon X. Wang  <https://orcid.org/0000-0002-6937-9034>
 R. Paul Butler  <https://orcid.org/0000-0003-1305-3761>
 Xavier Dumusque  <https://orcid.org/0000-0002-9332-2011>
 Jeffrey D. Crane  <https://orcid.org/0000-0002-5226-787X>
 Fabo Feng  <https://orcid.org/0000-0001-6039-0555>
 Benjamin T. Montet  <https://orcid.org/0000-0001-7516-8308>
 Adina D. Feinstein  <https://orcid.org/0000-0002-9464-8101>
 Erin Flowers  <https://orcid.org/0000-0001-8045-1765>
 Tansu Daylan  <https://orcid.org/0000-0002-6939-9211>
 Kevin I. Collins  <https://orcid.org/0000-0003-2781-3207>
 Dennis M. Conti  <https://orcid.org/0000-0003-2239-0567>
 Tianjun Gan  <https://orcid.org/0000-0002-4503-9705>
 Eric L. N. Jensen  <https://orcid.org/0000-0002-4625-7333>
 John F. Kielkopf  <https://orcid.org/0000-0003-0497-2651>
 Thiam-Guan Tan  <https://orcid.org/0000-0001-5603-6895>
 Ravit Helled  <https://orcid.org/0000-0001-5555-2652>
 Caroline Dorn  <https://orcid.org/0000-0001-6110-4610>
 Jonas Haldemann  <https://orcid.org/0000-0003-1231-2389>
 George R. Ricker  <https://orcid.org/0000-0003-2058-6662>
 Roland Vanderspek  <https://orcid.org/0000-0001-6763-6562>
 David W. Latham  <https://orcid.org/0000-0001-9911-7388>
 Joshua N. Winn  <https://orcid.org/0000-0002-4265-047X>
 Jon M. Jenkins  <https://orcid.org/0000-0002-8975-812X>
 Joseph D. Twicken  <https://orcid.org/0000-0002-6778-7552>
 Jeffrey C. Smith  <https://orcid.org/0000-0002-6148-7903>
 Peter Tenenbaum  <https://orcid.org/0000-0002-1949-4720>

Thomas Barclay  <https://orcid.org/0000-0001-7139-2724>
 Joshua Pepper  <https://orcid.org/0000-0002-3827-8417>
 William Fong  <https://orcid.org/0000-0003-0241-2757>

References

- Adams, F. C., & Laughlin, G. 2006, *ApJ*, **649**, 1004
- Astropy Collaboration, Robitaille, T. P., Tollerud, E. J., et al. 2013, *A&A*, **558**, A33
- Bailer-Jones, C. A. L., Rybizki, J., Fousneau, M., Mantelet, G., & Andrae, R. 2018, *AJ*, **156**, 58
- Bakos, G. Á., Torres, G., Pál, A., et al. 2010, *ApJ*, **710**, 1724
- Baranne, A., Queloz, D., Mayor, M., et al. 1996, *A&AS*, **119**, 373
- Barrado y Navascues, D., & Stauffer, J. R. 1996, *A&A*, **310**, 879
- Barragán, O., Aigrain, S., Kubyskhina, D., et al. 2019, *MNRAS*, **490**, 698
- Batalha, N. E., Lewis, T., Fortney, J. J., et al. 2019, *ApJL*, **885**, L25
- Beaugé, C., & Nesvorný, D. 2013, *ApJ*, **763**, 12
- Benneke, B., Knutson, H. A., Lothringer, J., et al. 2019, *NatAs*, **3**, 813
- Bensby, T., Feltzing, S., & Lundström, I. 2003, *A&A*, **410**, 527
- Bonfils, X., Gillon, M., Udry, S., et al. 2012, *A&A*, **546**, A27
- Bourrier, V., Lecavelier des Etangs, A., Ehrenreich, D., et al. 2018, *A&A*, **620**, A147
- Bovy, J., Rix, H.-W., Schlafly, E. F., et al. 2016, *ApJ*, **823**, 30
- Brown, T. M., Baliber, N., Bianco, F. B., et al. 2013, *PASP*, **125**, 1031
- Buchhave, L. A., Latham, D. W., Johansen, A., et al. 2012, *Natur*, **486**, 375
- Buchner, J. 2016, *S&C*, **26**, 383
- Burke, C. J., Bryson, S. T., Mullally, F., et al. 2014, *ApJS*, **210**, 19
- Butler, R. P., Marcy, G. W., Williams, E., et al. 1996, *PASP*, **108**, 500
- Butler, R. P., Vogt, S. S., Laughlin, G., et al. 2017, *AJ*, **153**, 208
- Butler, R. P., Vogt, S. S., Marcy, G. W., et al. 2004, *ApJ*, **617**, 580
- Cameron, A. C. 2012, *Natur*, **492**, 48
- Castelli, F., & Kurucz, R. L. 2004, in Proc. IAU Symp. 210, Modelling of Stellar Atmospheres, Poster Contributions, ed. N. Piskunov, W. W. Weiss, & D. F. Gray (San Francisco, CA: ASP), **A20**
- Cauley, P. W., Redfield, S., & Jensen, A. G. 2017, *AJ*, **153**, 81
- Chen, H., & Rogers, L. A. 2016, *ApJ*, **831**, 180
- Chiang, E., & Laughlin, G. 2013, *MNRAS*, **431**, 3444
- Choi, J., Dotter, A., Conroy, C., et al. 2016, *ApJ*, **823**, 102
- Ciardi, D. R., Beichman, C. A., Horch, E. P., & Howell, S. B. 2015, *ApJ*, **805**, 16
- Collins, K. A., Kielkopf, J. F., Stassun, K. G., & Hessman, F. V. 2017, *AJ*, **153**, 77
- Connolly, J. A. D. 2009, *GGG*, **10**, Q10014
- Coughlin, J. L., Mullally, F., Thompson, S. E., et al. 2016, *ApJS*, **224**, 12
- Crane, J. D., Shectman, S. A., & Butler, R. P. 2006, *Proc. SPIE*, **6269**, 626931
- Crane, J. D., Shectman, S. A., Butler, R. P., et al. 2010, *Proc. SPIE*, **7735**, 773553
- Crane, J. D., Shectman, S. A., Butler, R. P., Thompson, I. B., & Burley, G. S. 2008, *Proc. SPIE*, **7014**, 701479
- Cross, N. J. G., Collins, R. S., Mann, R. G., et al. 2012, *A&A*, **548**, A119
- Crossfield, I. J. M., & Kreidberg, L. 2017, *AJ*, **154**, 261
- Cruz, K. L., Reid, I. N., Liebert, J., Kirkpatrick, J. D., & Lowrance, P. J. 2003, *AJ*, **126**, 2421
- Cummings, J. D., Deliyannis, C. P., Maderak, R. M., & Steinhauer, A. 2017, *AJ*, **153**, 128
- Cutri, R. M., Skrutskie, M. F., van Dyk, S., et al. 2003, *yCat*, **2246**, 0
- Cutri, R. M., Wright, E. L., Conrow, T., et al. 2012, *yCat*, **2311**, 0
- Díaz, M. R., Jenkins, J. S., Gandolfi, D., et al. 2020, *MNRAS*, **493**, 973
- Dong, S., Xie, J.-W., Zhou, J.-L., Zheng, Z., & Luo, A. 2018, *PNAS*, **115**, 266
- Dorn, C., Venturini, J., Khan, A., et al. 2017, *A&A*, **597**, A37
- Dotter, A. 2016, *ApJS*, **222**, 8
- Dragomir, D., Teske, J., Günther, M. N., et al. 2019, *ApJL*, **875**, L7
- Duncan, D. K., Vaughan, A. H., Wilson, O. C., et al. 1991, *ApJS*, **76**, 383
- Eastman, J. 2017, EXOFASTv2: Generalized Publication-quality Exoplanet Modeling Code, Astrophysics Source Code Library, ascl:1710.003
- Eastman, J. D., Rodriguez, J. E., Agol, E., et al. 2019, arXiv:1907.09480
- Ehrenreich, D., Bourrier, V., Wheatley, P. J., et al. 2015, *Natur*, **522**, 459
- ESA 1997, The HIPPARCOS and TYCHO Catalogs. Astrometric and Photometric Star Catalogs Derived from the ESA HIPPARCOS Space Astrometry Mission, Vol. 1200 (Noordwijk: ESA)
- Esposito, M., Armstrong, D. J., Gandolfi, D., et al. 2019, *A&A*, **623**, A165
- Feinstein, A. D., Montet, B. T., Ansdell, M., et al. 2020, arXiv:2005.07710
- Feng, F., Lisogorskiy, M., Jones, H. R. A., et al. 2019, *ApJS*, **244**, 39
- Finch, C. T., Henry, T. J., Subasavage, J. P., Jao, W.-C., & Hambly, N. C. 2007, *AJ*, **133**, 2898
- Follert, R., Dorn, R. J., Oliva, E., et al. 2014, *Proc. SPIE*, **9147**, 914719
- Fortney, J. J. 2005, *MNRAS*, **364**, 649
- Fraine, J., Deming, D., Benneke, B., et al. 2014, *Natur*, **513**, 526
- Fulton, B. J. 2017, PhD thesis, Univ. of Hawai'i at Manoa
- Fulton, B. J., & Petigura, E. A. 2018, *AJ*, **156**, 264
- Fulton, B. J., Petigura, E. A., Howard, A. W., et al. 2017, *AJ*, **154**, 109
- Gaia Collaboration, Brown, A. G. A., Vallenari, A., et al. 2018, *A&A*, **616**, A1
- Ginzburg, S., Schlichting, H. E., & Sari, R. 2018, *MNRAS*, **476**, 759
- Girard, T. M., van Alena, W. F., Zacharias, N., et al. 2011, *AJ*, **142**, 15
- Günther, M. N., Pozuelos, F. J., Dittmann, J. A., et al. 2019, *NatAs*, **3**, 1099
- Hadden, S., & Lithwick, Y. 2017, *AJ*, **154**, 5
- Hakim, K., Rivoldini, A., Van Hoolst, T., et al. 2018, *Icar*, **313**, 61
- Hansen, B. M. S., & Barman, T. 2007, *ApJ*, **671**, 861
- Haywood, M., Di Matteo, P., Lehnert, M. D., Katz, D., & Gómez, A. 2013, *A&A*, **560**, A109
- Henden, A. A., Levine, S., Terrell, D., & Welch, D. L. 2015, AAS Meeting Abstracts, **225**, 336.16
- Henden, A. A., Templeton, M., Terrell, D., et al. 2016, *yCat*, **2336**, 0
- Høg, E., Fabricius, C., Makarov, V. V., et al. 2000, *A&A*, **355**, L27
- Hsu, D. C., Ford, E. B., Ragozzine, D., & Ashby, K. 2019, *AJ*, **158**, 109
- Jenkins, J. M., Twicken, J. D., McCauliff, S., et al. 2016, *Proc. SPIE*, **9913**, 99133E
- Jensen, A. G., Cauley, P. W., Redfield, S., Cochran, W. D., & Endl, M. 2018, *AJ*, **156**, 154
- Jensen, A. G., Redfield, S., Endl, M., et al. 2012, *ApJ*, **751**, 86
- Jensen, E. 2013, Tapir: A Web Interface for Transit/eclipse Observability, Astrophysics Source Code Library, ascl:1306.007
- Jiang, Y.-F., & Tremaine, S. 2010, *MNRAS*, **401**, 977
- Jin, S., & Mordasini, C. 2018, *ApJ*, **853**, 163
- Jin, S., Mordasini, C., Parmentier, V., et al. 2014, *ApJ*, **795**, 65
- Jones, B. F., Fischer, D., Shetrone, M., & Soderblom, D. R. 1997, *AJ*, **114**, 352
- Kempton, E. M.-R., Bean, J. L., Louie, D. R., et al. 2018, *PASP*, **130**, 114401
- Kostov, V. B., Orosz, J. A., Feinstein, A. D., et al. 2020, *AJ*, **159**, 253
- Kostov, V. B., Schlieder, J. E., Barclay, T., et al. 2019, *AJ*, **158**, 32
- Lallement, R., Capitanio, L., Ruiz-Dern, L., et al. 2018, *A&A*, **616**, A132
- Lecavelier Des Etangs, A. 2007, *A&A*, **461**, 1185
- Lenzen, R., Hartung, M., Brandner, W., et al. 2003, *Proc. SPIE*, **4841**, 944
- Li, J., Tenenbaum, P., Twicken, J. D., et al. 2019, *PASP*, **131**, 024506
- Lissauer, J. J., Ragozzine, D., Fabrycky, D. C., et al. 2011, *ApJS*, **197**, 8
- Lopez, E. D. 2017, *MNRAS*, **472**, 245
- Lopez, E. D., & Fortney, J. J. 2013, *ApJ*, **776**, 2
- Lopez, E. D., & Fortney, J. J. 2014, *ApJ*, **792**, 1
- Lopez, E. D., Fortney, J. J., & Miller, N. 2012, *ApJ*, **761**, 59
- Lundkvist, M. S., Kjeldsen, H., Albrecht, S., et al. 2016, *NatCo*, **7**, 11201
- Mamajek, E. E., Bartlett, J. L., Seifahrt, A., et al. 2013, *AJ*, **146**, 154
- Mann, A. W., Dupuy, T., Kraus, A. L., et al. 2019, *ApJ*, **871**, 63
- Marcy, G. W., & Butler, R. P. 1992, *PASP*, **104**, 270
- Matsumoto, Y., & Kokubo, E. 2017, *AJ*, **154**, 27
- Mayor, M., Pepe, F., Queloz, D., et al. 2003, *Msngr*, **114**, 20
- Mayor, M., & Queloz, D. 1995, *Natur*, **378**, 355
- Mazeh, T., Holczer, T., & Faigler, S. 2016, *A&A*, **589**, A75
- McDonald, G. D., Kreidberg, L., & Lopez, E. 2019, *ApJ*, **876**, 22
- Morley, C. V., Fortney, J. J., Marley, M. S., et al. 2015, *ApJ*, **815**, 110
- Morley, C. V., Knutson, H., Line, M., et al. 2017, *AJ*, **153**, 86
- Morris, R. L., Twicken, J. D., Smith, J. C., et al. 2017, Kepler Data Processing Handbook: Photometric Analysis, Kepler Science Document, **KSCI-19081-002**
- Morton, T. D. 2015, Isochrones: Stellar Model Grid Package, Astrophysics Source Code Library, ascl:1503.010
- Nave, G. 2017, in ESO Calibration Workshop: The Second Generation VLT Instruments and Friends (Garching: ESO), **32**
- Nelson, B. E., Ford, E. B., & Rasio, F. A. 2017, *AJ*, **154**, 106
- Ninan, J. P., Stefansson, G., Mahadevan, S., et al. 2020, *ApJ*, **894**, 97
- Ning, B., Wolfgang, A., & Ghosh, S. 2018, *ApJ*, **869**, 5
- Oklopčić, A. 2019, *ApJ*, **881**, 133
- Oklopčić, A., & Hirata, C. M. 2018, *ApJL*, **855**, L11
- Owen, J. E., & Jackson, A. P. 2012, *MNRAS*, **425**, 2931
- Owen, J. E., & Wu, Y. 2013, *ApJ*, **775**, 105
- Owen, J. E., & Wu, Y. 2017, *ApJ*, **847**, 29
- Paxton, B., Cantiello, M., Arras, P., et al. 2013, *ApJS*, **208**, 4
- Paxton, B., Marchant, P., Schwab, J., et al. 2015, *ApJS*, **220**, 15
- Pepe, F., Mayor, M., Rupprecht, G., et al. 2002, *Msngr*, **110**, 9
- Pepe, F., Molaro, P., Cristiani, S., et al. 2014, *AN*, **335**, 8
- Petigura, E. A., Marcy, G. W., Winn, J. N., et al. 2018, *AJ*, **155**, 89
- Ricker, G. R., Winn, J. N., Vanderspek, R., et al. 2015, *JATIS*, **1**, 014003
- Roussel, G., Lacombe, F., Puget, P., et al. 2003, *Proc. SPIE*, **4839**, 140

- Salz, M., Czesla, S., Schneider, P. C., et al. 2018, *A&A*, **620**, A97
- Sanchis-Ojeda, R., Rappaport, S., Winn, J. N., et al. 2014, *ApJ*, **787**, 47
- Saumon, D., Chabrier, G., & van Horn, H. M. 1995, *ApJS*, **99**, 713
- Schlegel, D. J., Finkbeiner, D. P., & Davis, M. 1998, *ApJ*, **500**, 525
- Schlichting, H. E., Sari, R., & Yalinewich, A. 2015, *Icar*, **247**, 81
- Schönrich, R., Binney, J., & Dehnen, W. 2010, *MNRAS*, **403**, 1829
- Seager, S., Kuchner, M., Hier-Majumder, C. A., & Militzer, B. 2007, *ApJ*, **669**, 1279
- Sestito, P., Randich, S., Mermilliod, J. C., & Pallavicini, R. 2003, *A&A*, **407**, 289
- Smith, J. C., Stumpe, M. C., Van Cleve, J. E., et al. 2012, *PASP*, **124**, 1000
- Snedden, C., Bean, J., Ivans, I., Lucatello, S., & Sobek, J. 2012, MOOG: LTE line Analysis and Spectrum Synthesis, Astrophysics Source Code Library, ascl:1202.009
- Snedden, C. A. 1973, PhD thesis, The Univ. of Texas
- Soto, M. G., & Jenkins, J. S. 2018, *A&A*, **615**, A76
- Spake, J. J., Sing, D. K., Evans, T. M., et al. 2018, *Natur*, **557**, 68
- Stassun, K. G., Collins, K. A., & Gaudi, B. S. 2017, *AJ*, **153**, 136
- Stassun, K. G., Corsaro, E., Pepper, J. A., & Gaudi, B. S. 2018, *AJ*, **155**, 22
- Stassun, K. G., Oelkers, R. J., Paegert, M., et al. 2019, *AJ*, **158**, 138
- Stassun, K. G., & Torres, G. 2016, *AJ*, **152**, 180
- Stassun, K. G., & Torres, G. 2018, *ApJ*, **862**, 61
- Stixrude, L., & Lithgow-Bertelloni, C. 2011, *GeoJI*, **184**, 1180
- Stumpe, M. C., Smith, J. C., Catanzarite, J. H., et al. 2014, *PASP*, **126**, 100
- Stumpe, M. C., Smith, J. C., Van Cleve, J. E., et al. 2012, *PASP*, **124**, 985
- Szabó, G. M., & Kiss, L. L. 2011, *ApJL*, **727**, L44
- Tokovinin, A., Fischer, D. A., Bonati, M., et al. 2013, *PASP*, **125**, 1336
- Twicken, J. D., Catanzarite, J. H., Clarke, B. D., et al. 2018, *PASP*, **130**, 064502
- Twicken, J. D., Clarke, B. D., Bryson, S. T., et al. 2010, *Proc. SPIE*, **7740**, 774023
- Van Eylen, V., & Albrecht, S. 2015, *ApJ*, **808**, 126
- Vazan, A., Kovetz, A., Podolak, M., & Helled, R. 2013, *MNRAS*, **434**, 3283
- Venturini, J., & Helled, R. 2017, *ApJ*, **848**, 95
- West, R. G., Gillen, E., Bayliss, D., et al. 2019, *MNRAS*, **486**, 5094
- Winters, J. G., Henry, T. J., Jao, W.-C., et al. 2011, *AJ*, **141**, 21
- Wolfgang, A., Rogers, L. A., & Ford, E. B. 2016, *ApJ*, **825**, 19
- Yan, F., & Henning, T. 2018, *NatAs*, **2**, 714
- Yee, S. W., Petigura, E. A., & von Braun, K. 2017, *ApJ*, **836**, 77
- Zahnle, K. J., & Catling, D. C. 2017, *ApJ*, **843**, 122
- Zeng, L., Jacobsen, S. B., Sasselov, D. D., et al. 2019, *PNAS*, **116**, 9723
- Zeng, L., Sasselov, D. D., & Jacobsen, S. B. 2016, *ApJ*, **819**, 127